



## Effects of LGM sea surface temperature and sea ice extent on the isotope-temperature slope at polar ice core sites

Alexandre CAUQUOIN<sup>1</sup>, Ayako ABE-OUCHI<sup>2</sup>, Takashi OBASE<sup>2</sup>, Wing-Le CHAN<sup>3</sup>, André PAUL<sup>4</sup> and Martin WERNER<sup>5</sup>

- 5 <sup>1</sup>Institute of Industrial Science (IIS), The University of Tokyo, Kashiwa, Japan  
<sup>2</sup>Atmosphere and Ocean Research Institute (AORI), The University of Tokyo, Kashiwa, Japan  
<sup>3</sup>Research Center for Environmental Modeling and Application, Japan Agency for Marine-Earth Science and Technology (JAMSTEC), Yokohama, Japan  
<sup>4</sup>MARUM – Center for Marine Environmental Sciences and Department of Geosciences, University of Bremen, Bremen,  
10 Germany  
<sup>5</sup>Alfred Wegener Institute (AWI), Helmholtz Centre for Polar and Marine Sciences, Bremerhaven, Germany

*Correspondence to:* Alexandre Cauquoin (cauquoin@iis.u-tokyo.ac.jp)

**Abstract.** Stable water isotopes in polar ice cores are widely used to reconstruct past temperature variations over several orbital climatic cycles. One way to calibrate the isotope-temperature relationship is to apply the present-day spatial relationship as a  
15 surrogate for the temporal one. However, this method leads to large uncertainties because several factors like the sea surface conditions or the origin and the transport of water vapor influence the isotope-temperature temporal slope. In this study, we investigate how the sea surface temperature (SST), the sea ice extent and the strength of the Atlantic Meridional Overturning Circulation (AMOC) affect these temporal slopes in Greenland and Antarctica for Last Glacial Maximum (LGM, ~21 000 years ago) to preindustrial climate change. For that, we use the isotope-enabled atmosphere climate model ECHAM6-wiso,  
20 forced with a set of sea surface boundary condition datasets based on reconstructions (e.g., GLOMAP) or MIROC 4m simulation outputs. We found that the isotope-temperature temporal slopes in East Antarctic coastal areas are mainly controlled by the sea ice extent, while the sea surface temperature cooling affects more the temporal slope values inland. Mixed effects on isotope-temperature temporal slopes are simulated in West Antarctica with sea surface boundary conditions changes, because the transport of water vapor from the Southern Ocean to this area can dampen the influence of temperature on the  
25 changes of the isotopic composition of precipitation and snow. In the Greenland area, the isotope-temperature temporal slopes are influenced by the sea surface temperatures very near the coasts of the continent. The greater the LGM cooling off the coast of southeast Greenland, the larger the temporal slopes. The presence or absence of sea ice very near the coast has a large influence in Baffin Bay and the Greenland Sea and influences the slopes at some inland ice cores stations. We emphasize that the extent far south of the sea ice is not so important. On the other hand, the seasonal variations of sea ice distribution, especially  
30 its retreat in summer, influence the water vapor transport in this region and the modeled isotope-temperature temporal slopes in the eastern part of Greenland. A stronger LGM AMOC decreases LGM to preindustrial isotopic anomalies in precipitation in Greenland, degrading the isotopic model-data agreement. The AMOC strength does not modify the temporal slopes over



inner Greenland, and only a little on the coasts along the Greenland Sea where the changes in surface temperature and sea ice distribution due to the AMOC strength mainly occur.

## 35 1 Introduction

Stable isotopologues of water ( $\text{H}_2^{16}\text{O}$ ,  $\text{H}_2^{18}\text{O}$  and  $\text{HD}^{16}\text{O}$ , called hereafter stable water isotopes) are integrated tracers of climate processes occurring in diverse parts of the hydrological cycle (Craig and Gordon, 1965; Dansgaard, 1964). Because of their differences in mass and symmetries, an isotopic fractionation happens at each phase change of water. This process is reflected by a change in the water isotope ratio values, expressed hereafter in the usual  $\delta$  notation (as  $\delta^{18}\text{O}$  and  $\delta^2\text{H}$  with respect to the  
40 Vienna Standard Mean Ocean Water V-SMOW if not stated otherwise). As a result, water isotopes have been widely used to describe past variations of the Earth's climate. For example, their measurements in polar ice cores made it possible to reconstruct the temperature variations over several glacial-interglacial cycles (Jouzel et al., 2007; Jouzel, 2013, and references therein; NEEM Community Members, 2013).

For such a reconstruction, the present-day isotope-temperature spatial slope can be taken as a surrogate for the temporal  
45 gradient at a given site. For example, a spatial slope of  $0.80 \text{‰ } ^\circ\text{C}^{-1}$  for  $\delta^{18}\text{O}$  in Antarctica was calculated based on a compilation of measured surface temperatures and  $\delta^{18}\text{O}$  of snow at various locations in the continent (Masson-Delmotte et al., 2008). However, this method often leads to a large error in the temperature reconstructions because the temporal isotope-temperature slope depends on many factors like the sea surface temperature (SST) (Risi et al., 2010), the sea ice extent (Noone and Simmonds, 2004), the ice sheet elevation (Werner et al., 2018), the origin and the transport of water vapor (Casado et al.,  
50 2018). For example, it has been suggested that the relationship between temperature and the isotopic signature for warmer interglacial periods in East Antarctica can vary among ice core sites, with an error in the temperature reconstruction that can reach up to 100 % (Sime et al., 2009; Cauquoin et al., 2015). In Greenland, the use of the spatial relationship between the  $\delta^{18}\text{O}$  in Greenland ice core records and surface temperature to evaluate the local temperature variations during the last deglaciation leads to a large uncertainty of a factor of 2 (Jouzel, 1999; Buizert et al., 2014). Recently, Buizert et al. (2021) proposed a  
55 reconstruction of surface cooling in Antarctica during the Last Glacial Maximum (LGM, ~21 000 years ago) using borehole thermometry and firn properties of different ice cores. Based on these results, they proposed new estimates of temporal  $\delta^{18}\text{O}$ -temperature slopes at these ice core stations, varying from 0.8 to  $1.45 \text{‰ } ^\circ\text{C}^{-1}$ .

The LGM is a period with full glacial conditions and represents the beginning of the last deglaciation. It is one of the key climate periods chosen by the Paleoclimate Modeling Intercomparison Project (PMIP, Kageyama et al., 2018, 2021) because  
60 it allows to evaluate how well state-of-the-art models are able to simulate climate changes as large as those expected in the future. In addition to being very different from the preindustrial climate (PI), the LGM period also offers a wealth of isotope proxy data, including stable water isotopes in polar ice cores for an in-depth comparison with outputs from isotope-enabled models (Lee et al., 2008; Risi et al., 2010; Werner et al., 2016, 2018).



One way to capture the physical processes influencing the temporal isotope-temperature slope in polar regions is the use of  
65 Atmospheric General Circulation Models (AGCMs) equipped with prognostic stable water isotopes. Such models can simulate  
different climate conditions, like LGM and PI periods. Moreover, the use of isotope-enabled AGCMs in combination with  
isotopic observations allows us to investigate the physical processes controlling the variations of isotopic delta values at a  
given site. This method makes it possible to estimate the temporal isotope-temperature slope for LGM to preindustrial climate  
change (Lee et al., 2008; Risi et al., 2010; Werner et al., 2018). Even if such models simulate various temporal isotope-  
70 temperature slopes, implying that processes like water vapor transport, post-depositional effects, or polar atmospheric  
boundary layer are poorly or not represented (Krinner et al., 1997; Werner et al., 2000; Casado et al., 2018), these models are  
very useful for evaluating the sensitivity of the temporal slopes to parameters like the change of elevation (Werner et al., 2018).  
Ocean surface conditions are one of the factors that influences LGM-PI isotope changes (Risi et al., 2010; Noone and  
Simmonds, 2004). Two reconstructions of SST and one of sea ice extent during the LGM period have been released recently.  
75 Paul et al. (2021) reconstructed both the SST and the sea ice extent fields, based on faunal and floral assemblage data of the  
Multiproxy Approach for the Reconstruction of the Glacial Ocean Surface (MARGO) project and several recent estimates of  
the LGM sea ice extent. The Data-Interpolation Variational Analysis (DIVA) software was used to optimally interpolate sparse  
SST reconstruction data. The resulting reconstruction was called GLOMAP (Glacial Ocean Map). Tierney et al. (2020)  
reconstructed the LGM SST field with a different method, by combining a large collection of geochemical proxies for sea  
80 surface temperature with simulations outputs from the isotope-enabled model iCESM1.2 (Brady et al., 2019) using an offline  
data assimilation technique to produce a field reconstruction of LGM temperatures. Tierney et al. (2020) LGM cooling is  
globally larger than in GLOMAP (3.6°C and 1.7°C, respectively), with possible impacts on LGM to PI isotope changes and  
their temporal relationship with near surface air temperature. In addition, other SST and sea ice fields, with different  
characteristics compared to the reconstructions of LGM sea surface conditions described above, can be extracted from  
85 atmosphere-ocean coupled model simulations like MIROC 4m (Obase and Abe-Ouchi, 2019).

In the present study, we investigate the impacts of SST and sea ice boundary conditions on the isotope-temperature temporal  
slope at polar ice core sites for LGM-to-PI changes. For that, we performed multiple simulations with the isotope-enabled  
AGCM ECHAM6-wiso driven by different LGM SST and sea ice boundary conditions. We evaluate the modeled LGM-PI  
 $\delta^{18}\text{O}$  anomalies with available observations and we investigate how the SST and the sea ice extent patterns influence the model-  
90 data agreement on a global scale and at polar ice core stations. The influence of ocean circulation, particularly the strength of  
the Atlantic Meridional Overturning Circulation (AMOC), on sea surface conditions and by extension on our modeled  $\delta^{18}\text{O}$  of  
meteoric water is also investigated. Finally, the impacts of the sea surface boundary conditions on the  $\delta^{18}\text{O}$ -temperature slopes  
for LGM-to-preindustrial climate change are evaluated and discussed for Greenland and Antarctic ice core stations.



## 2 Methodology

### 95 2.1 ECHAM6-wiso

ECHAM6 (Stevens et al., 2013) is the sixth generation of the atmospheric general circulation model ECHAM, developed at the Max Planck Institute for Meteorology. It consists of a dry spectral-transform dynamical core, a transport model for scalar quantities other than temperature and surface pressure, a suite of physical parameterizations for the representation of diabatic processes, and boundary datasets for externalized parameters (trace gas and aerosol distributions, land surface properties, etc.).

100 ECHAM6 forms the atmospheric component of the fully coupled Earth system model MPI-ESM (Giorgetta et al., 2013; Mauritsen et al., 2019). The implementation of the water isotopes in ECHAM6 as part of MPI-ESM has been described and evaluated in detail by Cauquoin et al. (2019b), and this model version has been labeled ECHAM6-wiso. At a later stage, Cauquoin and Werner (2021) updated the water isotope module of ECHAM6-wiso in several aspects. The supersaturation has been slightly re-tuned, the kinetic fractionation factors for the evaporation over the ocean are now assumed as independent of

105 wind speed, and the isotopic content of snow on sea ice is taken into account for sublimation processes in sea ice covered regions. The latter leads to a stronger depletion of surface water vapor over such sea ice covered areas (while the surface temperature remains the same). As a consequence, this change is expected to contribute to a steeper temporal isotope-temperature slope over sea ice covered areas.

### 2.2 Sea surface temperature and sea ice extent boundary conditions for LGM conditions

#### 110 2.2.1 SST

Tierney et al. (2020) SST reconstruction has a larger and more homogeneous cooling than GLOMAP, except for the high southern latitudes at which the Pacific sector cools more than the Atlantic sector (Figure 1). On the other hand, the LGM cooling in the Northern North Atlantic Ocean is stronger in GLOMAP than in Tierney et al. reconstruction ( $-5.4^{\circ}\text{C}$  and  $-4.8^{\circ}\text{C}$ , respectively, see Table 4 in Paul et al., 2021). These differences between the two SST reconstructions are due to the use of

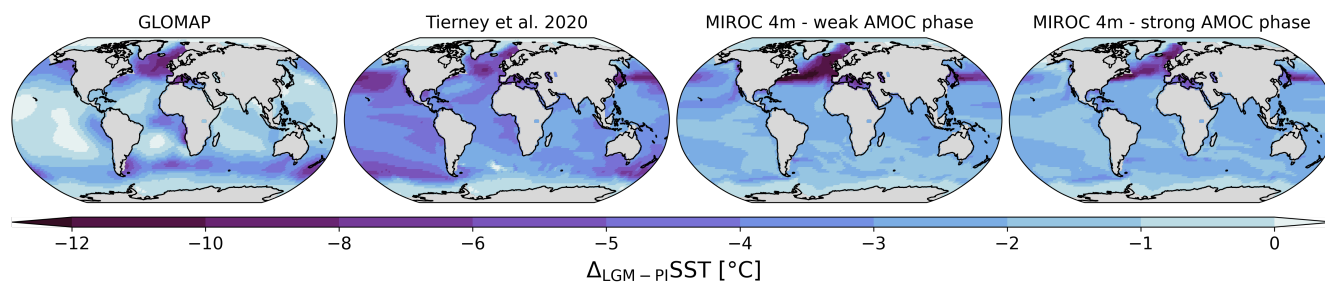
115 different proxy datasets for the reconstructions (geochemical proxies only for Tierney et al., MARGO dataset for GLOMAP) and to the methods applied to produce SST gridded maps from scattered observations (see Section 1). For their offline data assimilation technique, Tierney et al. (2020) used results from the coupled climate model iCESM1.2, which shows one of the largest cooling among the PMIP4 models (Figure 1b of Kageyama et al., 2021). In addition to these two reconstructions, we used SST and sea ice extent outputs from a MIROC 4m LGM simulation (Obase and Abe-Ouchi, 2019) with oscillating AMOC

120 strength. The global LGM cooling is between  $-2.3$  and  $-2.7^{\circ}\text{C}$  according to the considered simulations (Figure 1) i.e., higher than GLOMAP and lower than the Tierney et al. reconstruction. The main specificity of MIROC 4m LGM SST is a very strong cooling in the North Atlantic (more than  $10^{\circ}\text{C}$ , Figure 1) and more uniform temperature anomalies between  $-2$  and  $-4^{\circ}\text{C}$  in the other areas, including off the coast of Greenland. We extracted the MIROC 4m SST outputs, averaged over a 100-year period, at two different times of the LGM simulation depending on the AMOC strength: during a weak AMOC phase (average AMOC index was equal to 8.44 Sv) and a strong AMOC phase (19.95 Sv). A weaker AMOC during LGM implies larger cooling in

125



the North Atlantic (Figure 1) and more extended sea ice (Figure 2), while it does less cooling in the Southern Ocean. The strong AMOC phase period in MIROC 4m simulation was selected in the middle of the AMOC peak. Therefore, the values of MIROC 4m average near surface air temperature in Antarctica are very similar regardless the selected AMOC phase. For example, MIROC 4m simulates LGM temperature of  $-41.87$  and  $-41.75^{\circ}\text{C}$  in WDC station for strong and weak AMOC phase, respectively. A similar pattern is found for the eastern part of the continent ( $-56.80$  and  $-56.50^{\circ}\text{C}$  in Dome Fuji for strong and weak AMOC phase, respectively).



135 **Figure 1: LGM-PI sea surface temperature changes used as boundary conditions for ECHAM6-wiso simulations. From left to right: GLOMAP (Paul et al., 2021), Tierney et al. (2020), MIROC 4m with weak LGM AMOC phase and MIROC 4m with strong LGM AMOC phase.**

### 2.2.2 Sea ice extent

Maps of the averaged sea ice area fraction used as boundary forcings for ECHAM6-wiso are shown in Figure 2. The PI AMIP and LGM GLOMAP sea ice cover is higher around Antarctica compared to MIROC 4m ones, with a further extent in the Southern Ocean especially in the Atlantic sector. On the other hand, sea ice is more extensive in the Northern Hemisphere for MIROC 4m in the weak AMOC phase. For the stronger AMOC case, a decline of the sea ice in the Northern Hemisphere is seen, accompanied by weaker cooling (see section 2.2.1). In its parameterization, MIROC 4m uses a threshold of 95% for the sea ice fraction to allow sub-grid “sea-ice leads”. This threshold is not rigid, but it is difficult to exceed sea ice concentrations of 95% unless there is significant convergence of sea-ice. Consequently, while the sea ice is, on average, more extensive in the north in MIROC 4m for the weak AMOC phase compared to GLOMAP reconstruction, the sea ice area fraction in grid cells near coastal areas like Greenland is lower in MIROC 4m than in GLOMAP (95-98% against 100%, respectively).

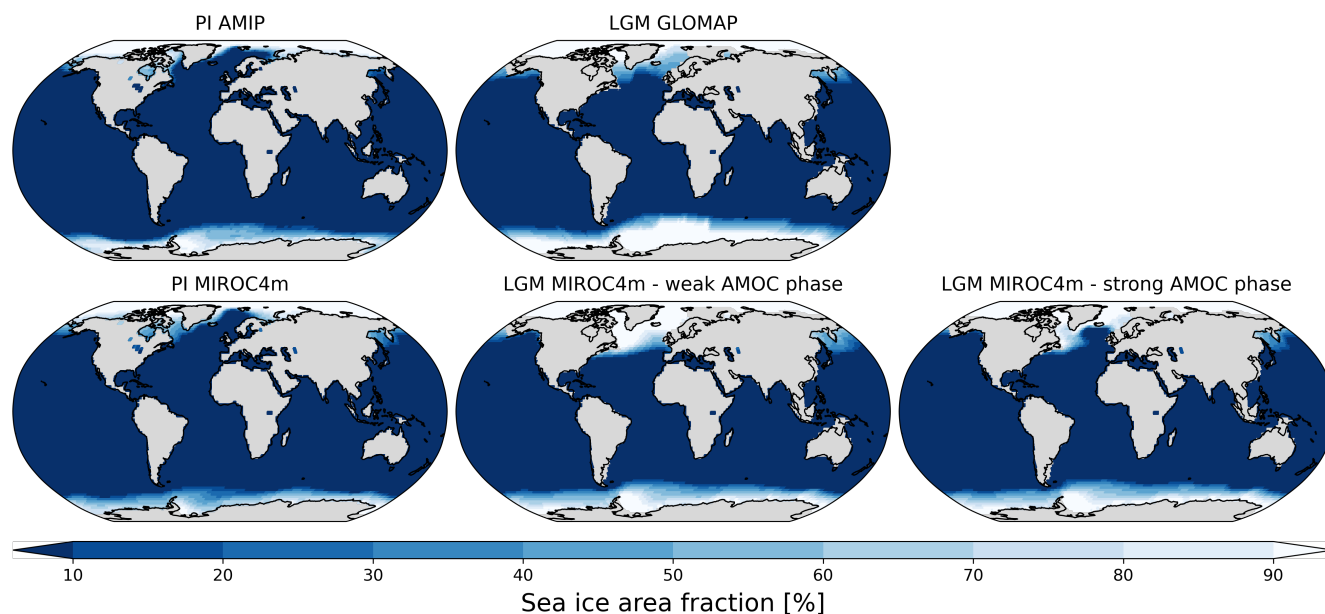


Figure 2: LGM and PI sea ice area fractions used as boundary conditions for ECHAM6-wiso simulations.

### 2.3 Model setup and experiments

We performed an ensemble of LGM simulations with ECHAM6-wiso, forced with different combinations of SST and sea ice  
150 boundary forcings presented in section 2.2. The LGM SST boundary fields are expressed relative to the AMIP mean SST  
(averaged over the period 1870 to 1899) used for the preindustrial simulations. The GLOMAP reconstruction has the advantage  
of providing a monthly climatology of LGM SST and sea ice extent, while only annual mean SST is available from the  
reconstruction by Tierney et al. (2020), without sea ice map distribution. So, Tierney et al. LGM SST for ECHAM6-wiso was  
produced by taking the annual mean SST anomaly from Tierney et al. (2020) and adopting the monthly climatology  
155 temperature variability from GLOMAP. We used the sea ice extent data from GLOMAP in this case, too. In order to investigate  
the impact of sea ice extent on our isotope results and the related isotope-temperature slopes for LGM-to-PI climate change,  
we used LGM SST outputs from MIROC 4m simulations combined with sea ice extent data from the same MIROC 4m  
simulations or from GLOMAP dataset. Similarly for PI conditions, we performed several PI simulations with different sea ice  
boundary conditions depending on the setup of LGM experiments, using climatological monthly mean sea ice area fractions  
160 from AMIP or MIROC 4m coupled simulations. The prescribed LGM ice sheet is GLAC-1D (Tarasov and Peltier, 2002;  
Tarasov et al., 2012, 2014; Abe-Ouchi et al., 2013; Briggs et al., 2014) for all LGM simulations. As with SST and sea ice  
distribution, mean  $\delta^{18}\text{O}$  of surface seawater needs to be prescribed. For the PI simulations, we used the  $\delta^{18}\text{O}$  reconstruction  
from the global gridded data set of LeGrande and Schmidt (2006). As no equivalent data set of the  $\delta^2\text{H}$  composition of seawater  
exists, the deuterium isotopic composition of the seawater in any grid cell has been set equal to the related  $\delta^{18}\text{O}$  composition,  
165 multiplied by a factor of 8, in accordance with the observed relation for meteoric water on a global scale (Craig, 1961). As in



Werner et al. (2018), a prescribed glacial seawater enrichment of +1 ‰ and +8‰ is assumed for  $\delta^{18}\text{O}$  and  $\delta^2\text{H}$  in the LGM simulations, respectively. Finally, the greenhouse gas and orbital conditions were prescribed according to PMIP4 protocol. The PI and LGM simulations were run for 60 and 120 model years, respectively, and we used the last 30 model years for our analyses. The simulations' characteristics are summarized in Table 1. Two additional sensitivity simulations have been performed to evaluate the impacts of lower MIROC 4m sea ice area fraction in coastal grid cells (section 2.2.2) and the consideration of the isotopic composition of snow on sea ice in ECHAM6-wiso (section 2.1) on the modeled  $\delta^{18}\text{O}_p$ -temperature temporal slopes between LGM and PI (see text in Supplementary Material). Also, a LGM simulation using the PMIP3 ice sheet reconstruction instead of GLAC-1D (see Figures 3b and 3d of Werner et al. (2018), respectively) has been performed to evaluate the impact of ice sheet topography on the isotopically enriched bias in Antarctica (see text in Supplementary Material).

175 **Table 1: Characteristics of the ECHAM6-wiso simulations in the present study.**

LGM simulation name	SST	Sea ice	PI control simulation characteristics	Comments
LGM_GLOMAP	GLOMAP	GLOMAP	Mean PI SST and sea ice from AMIP	Lower SST cooling
LGM_tierney2020	Tierney et al., 2020	GLOMAP	Mean PI SST and sea ice from AMIP	Higher SST cooling
LGM_miroc4m_sst_glomap_sic	MIROC 4m	GLOMAP	Mean PI SST and sea ice from AMIP	AMOC oscillation: weak phase
LGM_miroc4m_sst_and_sic	MIROC 4m	MIROC 4m	Mean PI SST from AMIP and PI sea ice from MIROC 4m	AMOC oscillation: weak phase
LGM_miroc4m_strong_AMOC_sst_glomap_sic	MIROC 4m	GLOMAP	Mean PI SST and sea ice from AMIP	AMOC oscillation: strong phase
LGM_miroc4m_strong_AMOC_sst_and_sic	MIROC 4m	MIROC 4m	Mean PI SST from AMIP and PI sea ice from MIROC 4m	AMOC oscillation: strong phase

## 2.4 Observational data

To evaluate the modeled  $\delta^{18}\text{O}$  of precipitation and snow values at ice core stations, we use here a selection of 6 Greenland and 10 Antarctic ice cores for the preindustrial and LGM climates (Figure 3). The observed  $\delta^{18}\text{O}$  values were defined as averages over the last 200 years for the preindustrial period, and in the  $21 \pm 1$  ka period for the LGM. We also use LGM-PI  $\delta^{18}\text{O}$  anomalies from 5 (sub-)tropical ice cores that are reported in Table 2 of Risi et al. (2010). The ice core data used in this study are summarized in Table 2. In order to mitigate the seasonal bias when comparing observed  $\delta^{18}\text{O}$  from snow in ice cores with modeled  $\delta^{18}\text{O}$  of precipitation or deposited snow, the modeled  $\delta$  values are calculated as a precipitation (or snow)-weighted mean with respect to the V-SMOW scale. For the evaluation of modeled  $\delta^{18}\text{O}$  of precipitation at a global spatial scale, we extracted 14 entities from the SISALv2 speleothem dataset (Comas-Bru et al., 2020) where both PI and LGM  $\delta^{18}\text{O}$  values of calcite or aragonite are available. As recommended by Comas-Bru et al. (2019), we defined here averaged PI and LGM values as the means of the 1850-1990 CE and  $21 \pm 1$  ka periods, respectively. To compare the  $\delta^{18}\text{O}$  of speleothem data with our modeled  $\delta^{18}\text{O}$  of precipitation ( $\delta^{18}\text{O}_p$ ), the measured  $\delta^{18}\text{O}$  of calcite or aragonite are converted into  $\delta^{18}\text{O}$  of drip-water using equations 1 or 2 of Comas-Bru et al. (2019), respectively, after conversion from V-PDB to VSMOW scale (equation 3 of



Comas-Bru et al. (2019)). The annual mean surface air temperature from ECHAM6-wiso is used for the conversion. A seasonal  
190 bias can appear in the isotopic composition of drip water archived in speleothem records due to the re-evaporation of the  
precipitated water (Wackerbarth et al., 2010). An additional fractionation between the drip water and the formed  
calcite/aragonite can also be observed for many speleothems (Dreybrodt and Scholz, 2011).

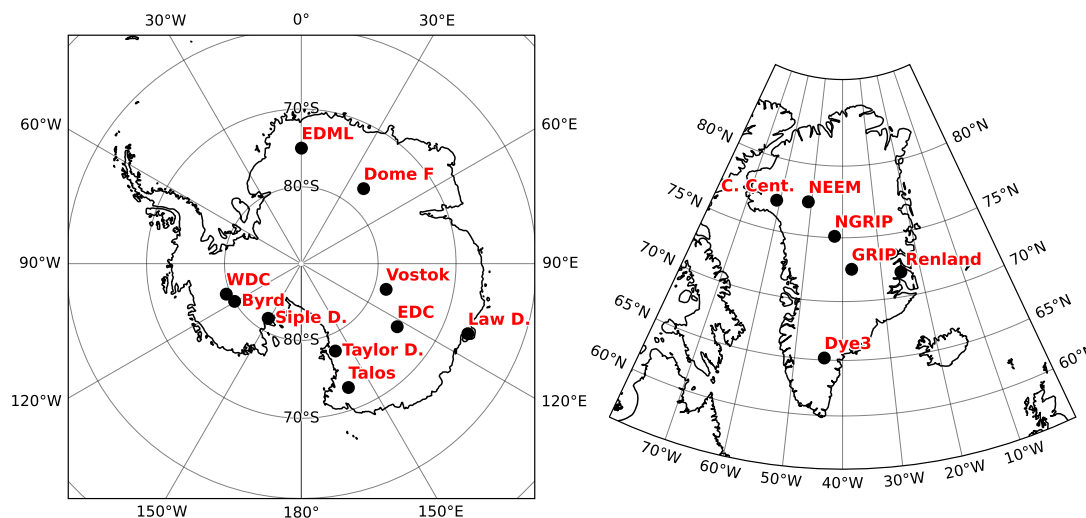


Figure 3: Location of polar ice core sites in Antarctica (left) and Greenland (right).

195

200

205





210 **Table 2: Selected ice cores records and their geographical coordinates, reported PI values of  $\delta^{18}\text{O}$  and changes in  $\delta^{18}\text{O}$  between LGM and PI.**

Site	Longitude	Latitude	$\delta^{18}\text{O}_{\text{PI}}$ (‰)	$\Delta_{\text{LGM-PI}}\delta^{18}\text{O}$ (‰)
Vostok <sup>a,b</sup>	106.87	-78.47	-56.8	-4.8
Dome F <sup>c</sup>	39.70	-77.32	-54.6	-4.9
EDC <sup>d,e</sup>	123.35	-75.10	-50.4	-5.6
EDML <sup>b,d</sup>	0.07	-75.00	-44.8	-6.3
Law Dome <sup>b</sup>	112.83	-66.73	-22.4	-5.5
Taylor Dome <sup>f</sup>	158.72	-77.8	-40.5	-3.5
Talos <sup>g</sup>	159.18	-72.82	-36.1	-5.4
Byrd <sup>h</sup>	-119.52	-80.02	-32.9	-7.3
Siple Dome <sup>b</sup>	-148.82	-81.67	-25.6	-7.8
WDC <sup>b</sup>	-112.14	-79.46	-34	-7.3
GRIP <sup>a,j</sup>	-37.63	72.58	-35.3	-5.4
NGRIP <sup>a,k</sup>	-42.32	75.10	-35.2	-7.4
NEEM <sup>l,m</sup>	-51.06	77.45	-33	-10
Camp Century <sup>i</sup>	-61.13	77.17	-29.3	-12.9
Dye3 <sup>j</sup>	-43.81	65.18	-27.7	-7.3
Renland <sup>i</sup>	-25.00	72.00	-27.4	-3.8
Huascarán <sup>a</sup>	-77.61	-9.11	-	-6.3
Sajama <sup>a</sup>	-68.97	-18.1	-	-5.4
Illimani <sup>a</sup>	-67.77	-16.62	-	-6
Guliyá <sup>a</sup>	81.48	35.28	-	-5.4
Dunde <sup>a</sup>	96	38	-	-2

References: <sup>a</sup> reported in Risi et al. (2010), <sup>b</sup> WAIS Divide project members (2013), <sup>c</sup> Kawamura et al. (2007), <sup>d</sup> Stenni et al. (2010), <sup>e</sup> Landais et al. (2015), <sup>f</sup> Steig et al. (2000), <sup>g</sup> Stenni et al. (2011), <sup>h</sup> Blunier and Brook (2001), <sup>i</sup> Vinther et al. (2009), <sup>j</sup> Vinther et al. (2006), <sup>k</sup> North Greenland Ice Core project members (2004), <sup>l</sup> Guillevic et al. (2013), <sup>m</sup> Schüpbach et al. (2018).

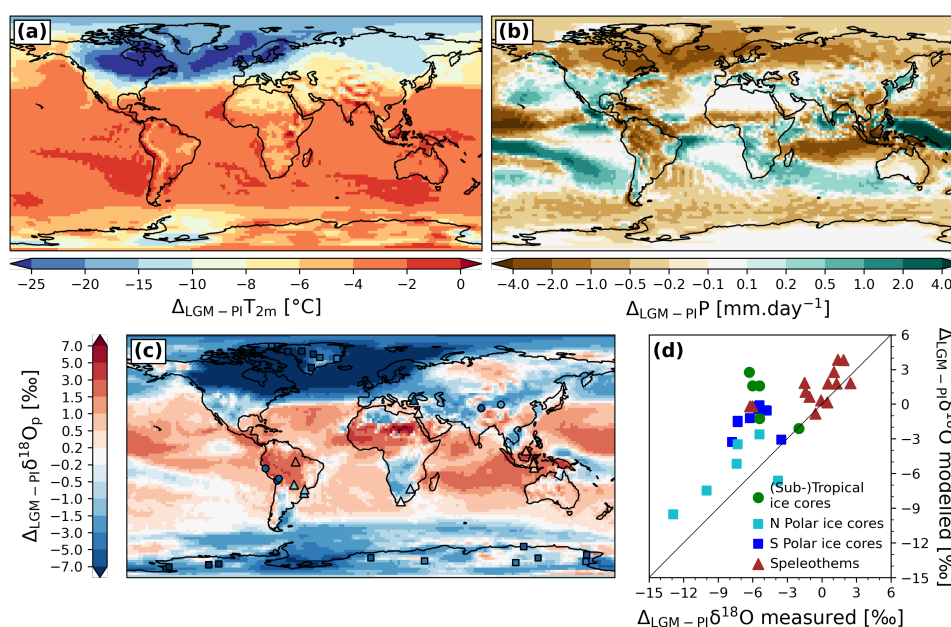
### 3 Results of the LGM-PI ECHAM6-wiso simulations

#### 215 3.1 Evaluation of ECHAM6-wiso under LGM conditions

We evaluate here the global distribution of  $\delta^{18}\text{O}_p$  changes between LGM and PI ( $\Delta_{\text{LGM-PI}}\delta^{18}\text{O}_p$ ) from our different ECHAM6-wiso simulations. Figure 4 shows the comparison of modeled  $\delta^{18}\text{O}_p$  anomalies with isotope measurements from ice cores and speleothems for the simulation LGM\_miroc4m\_sst\_and\_sic (i.e., SST and sea ice boundary conditions from MIROC 4m simulation at weak AMOC phase). Well-known patterns of global  $\Delta_{\text{LGM-PI}}\delta^{18}\text{O}_p$  distribution are found in ECHAM6-wiso, like  
 220 the negative anomalies across Canada, Greenland and Northern Europe due to the presence of glaciers in these areas during



LGM period (Figure 4c). Generally, negative  $\delta^{18}\text{O}_p$  anomalies are also simulated over Antarctica and the Southern Ocean due to lower temperatures in LGM compared to PI period (Figure 4a). In the mid-to-low latitudes,  $\Delta_{\text{LGM-PI}}\delta^{18}\text{O}_p$  is mainly controlled by precipitation anomalies (Figure 4b). For example, lower modeled precipitation in the Amazonian area, over parts of South East Asia and in the western Pacific Ocean during the LGM leads to positive modeled  $\delta^{18}\text{O}_p$  anomalies. Despite some biases in modeled  $\Delta_{\text{LGM-PI}}\delta^{18}\text{O}_p$ , like in Southern Amazonia (Figures 4c and d) where negative anomalies are measured in ice cores (between -2 and -6‰, see green dots in Figure 4d) while positive anomalies are simulated (between 0 and 4‰), modeled  $\delta^{18}\text{O}_p$  anomalies are in rather good agreement with observations from ice cores and speleothems (Figure 4d).



230 **Figure 4: Changes in modeled (a) 2m air temperature, (b) precipitation and (c)  $\delta^{18}\text{O}_p$  between the LGM and PI climates from the LGM\_miroc4m\_sst\_and\_sic simulation (background colors). In (c), the squares, dots and triangles represent  $\delta^{18}\text{O}$  changes measured in polar ice cores, (sub-)tropical ice cores and speleothems, respectively. Measured  $\delta^{18}\text{O}$  in calcite or aragonite from speleothems have been converted into  $\delta^{18}\text{O}$  of drip-water before comparison with modeled  $\delta^{18}\text{O}_p$  (see Section 2.4). (d) Scatter plot showing a comparison of observed  $\delta^{18}\text{O}$  changes with modeled  $\delta^{18}\text{O}_p$  anomalies at the nearest grid cell of the archives' locations. Northern and southern polar ice core locations are distinguished by cyan and blue colors, respectively.**

235 The isotope distribution is mainly controlled by changes in temperature and in the water cycle. Even though all the ECHAM6-wiso simulations show similar global distribution of 2m air temperature ( $T_{2m}$ ) and precipitation responses to the various SST and sea ice boundary fields, we find some differences too (Figures S1 and S2 in Supplementary Material). As expected, the modeled global cooling using SST from GLOMAP is lower while it is stronger when using SST from Tierney et al. (2020) (cooling of -4 and -6.3°C, respectively). Average  $T_{2m}$  anomalies in the middle range are obtained when using the MIROC 4m  
240 SST fields (between -4.4 and -5.3°C depending on the MIROC 4m data used). The temperature over sea ice covered areas are largely impacted by the sea ice forcings used (i.e., GLOMAP or MIROC 4m). The modeled  $T_{2m}$  anomalies over the Southern Ocean vary between -10 and -15°C with GLOMAP sea ice while the cooling is only between -4 and -10°C when ECHAM6-



wiso is forced by MIROC 4m sea ice. The opposite is true for the Arctic region. A strong cooling is simulated with the sea ice from MIROC 4m with a weak AMOC phase (a cooling of more than 20°C), more than with the sea ice from GLOMAP (between -20 and -10°C). The different SST boundary conditions have a strong influence on the precipitation anomalies, especially at mid-to-low latitudes including the western Pacific area and the East Asian monsoon region (Figure S2). All these differences in  $T_{2m}$  and precipitation responses have profound impacts on modeled  $\delta^{18}O_p$  anomalies (Figure S3) and their agreements with observations (Figures 4c and d).

**Table 3: Values of  $\Delta_{LGM-PI}\delta^{18}O$  model-data slope (1 is better), coefficient of determination  $r^2$  and root mean square error (RMSE) for our ECHAM6-wiso simulations using different SST and sea ice boundary fields. For each column, worst to best model-data agreements are shown with a yellow-to-green colormap.**

LGM simulation name	Slope	$r^2$	RMSE (‰)
LGM_GLOMAP	0.699	0.540	3.943
LGM_tierney2020	0.646	0.584	3.507
LGM_miroc4m_sst_glomap_sic	0.592	0.562	3.907
LGM_miroc4m_sst_and_sic	0.582	0.498	4.135
LGM_miroc4m_strong_AMOC_sst_glomap_sic	0.660	0.580	3.910
LGM_miroc4m_strong_AMOC_sst_and_sic	0.558	0.532	4.299

The statistics of  $\Delta_{LGM-PI}\delta^{18}O_p$  model-data agreements are shown for our different ECHAM6-wiso simulations in Table 3. The best model-data agreement in terms of model-data slope (1 is perfect match) is found when using SST and sea ice from GLOMAP (slope = 0.70) as boundary conditions for ECHAM6-wiso, but better coefficient of determination ( $r^2$ ) and root mean square error (RMSE) are obtained with LGM SST from Tierney et al. (2020) ( $r^2 = 0.58$  and RMSE = 3.5 ‰). We notice a worse model-data agreements in  $\delta^{18}O_p$  changes when both SST and sea ice changes from MIROC 4m simulations are provided as sea surface boundary conditions (slopes lower than 0.582 and RMSE higher than 4.1 ‰). This is in agreement with Werner et al. (2018) who showed a worse model-data agreement when using SST and sea ice boundary conditions from a coupled model instead of reconstructed ones. The substitution of MIROC 4m sea ice changes by GLOMAP ones improves the  $\Delta_{LGM-PI}\delta^{18}O_p$  model-data agreement for all cases (i.e., weak or strong AMOC phase). For example, the model-data slope when using SST changes from MIROC 4m simulation during strong AMOC phase is similar to the one for the simulation with the Tierney et al. SST reconstruction (0.66 and 0.65, respectively).

### 3.2 Impacts of SST boundary conditions on the $\Delta_{LGM-PI}\delta^{18}O$ model-data agreement at polar ice core stations

The modeled values of  $\Delta_{LGM-PI}\delta^{18}O$  of snow ( $\delta^{18}O_{sn}$ ) at polar ice cores stations for different boundary conditions in LGM-PI SST changes are compared to isotopic observations in Figure 5a. Only simulations using sea ice from GLOMAP are selected here. Except for Renland station in the North and Taylor Dome in the South (that are both coastal sites), ECHAM6-wiso generally under-estimates  $\delta^{18}O_{sn}$  changes. The main explanation for this general bias is the use of GLAC-1D ice sheet



reconstruction for our ECHAM6-wiso simulations. The substitution of GLAC-1D reconstruction by the PMIP3 one strongly  
270 improves the model-data agreement of  $\delta^{18}\text{O}$  in Antarctica (Figure S4), leading to a better model-data agreement at global scale  
(slope = 0.87,  $r^2 = 0.62$  and RMSE = 3.2 ‰) compared to the LGM\_GLOMAP experiment. This agrees with the findings of  
Werner et al. (2018) who showed that the isotopic model-data correlation for Antarctic ice core stations is weaker when using  
GLAC-1D instead of PMIP3 ice sheet reconstruction (RMSE = 2.1 and 1.1 ‰ for 11 Antarctic stations, respectively). Except  
for the Taylor Dome station, all modeled  $\Delta_{\text{LGM-PI}}\delta^{18}\text{O}_{\text{sn}}$  at polar ice core stations are in better agreement with measurements  
275 (blue bars in Figure 5a) when SST fields from GLOMAP or Tierney et al. are used (orange and green bars in Figure 5a,  
respectively), confirming the results of Werner et al. (2018) about the worse model-data agreement when using sea surface  
boundary conditions from a coupled model instead of reconstructed ones. The change from one MIROC 4m SST field to  
another one (i.e., weak or strong AMOC phase) as input for ECHAM6-wiso does not modify the modeled  $\Delta_{\text{LGM-PI}}\delta^{18}\text{O}_{\text{sn}}$  values  
much (red and purple bars in Figure 5a).

280 As expected, the modeled cooling is globally lower when using SST from GLOMAP to drive ECHAM6-wiso (left maps in  
subplots (c) to (e) of Figure 5). However, a strong cooling is obtained with GLOMAP SST in the Southern Ocean, which is  
the evaporative source of isotopic signals measured in polar areas. As a consequence, temperature changes in Antarctica are  
stronger when using SST from GLOMAP or Tierney et al., giving higher modeled  $\delta^{18}\text{O}_{\text{p}}$  changes compared to modeled results  
using SST fields from MIROC 4m (right maps of Figure 5), and better agreement with the observations. The stronger cooling  
285 in the Atlantic sector of the Southern Ocean with GLOMAP SST compared to Tierney et al. one has the consequence of  
enhancing the  $\delta^{18}\text{O}_{\text{p}}$  depletion in the Atlantic-Indian Ocean sector of Antarctica (right map of Figure 5c) despite similar  
temperatures between the two simulations (left map of Figure 5c). This area includes the ice core stations Dome Fuji and  
EDML, and a better model-data agreement is found there when GLOMAP SST values are provided as boundary conditions  
(Figure 5a). The opposite is true for other stations further to the east and west, like WDC and EDC. As in the Southern Ocean,  
290 a higher cooling is simulated in the Northern North Atlantic Ocean to the south of Greenland if the SST from GLOMAP is  
used. A stronger cooling is simulated in the southern and central part of inner Greenland, too (left maps of Figure 5). As a  
consequence, higher  $\delta^{18}\text{O}$  changes between LGM and PI are simulated in Greenland with the SST from GLOMAP (right maps  
of Figure 5), except in Northern Greenland like at Camp Century station (Figure 5a). A better agreement is obtained with the  
Greenland  $\delta^{18}\text{O}$  observations under this configuration (orange bars in Figure 5a), except for Renland and Camp Century (worse  
295 and similar model-data agreements among the simulation results, respectively).

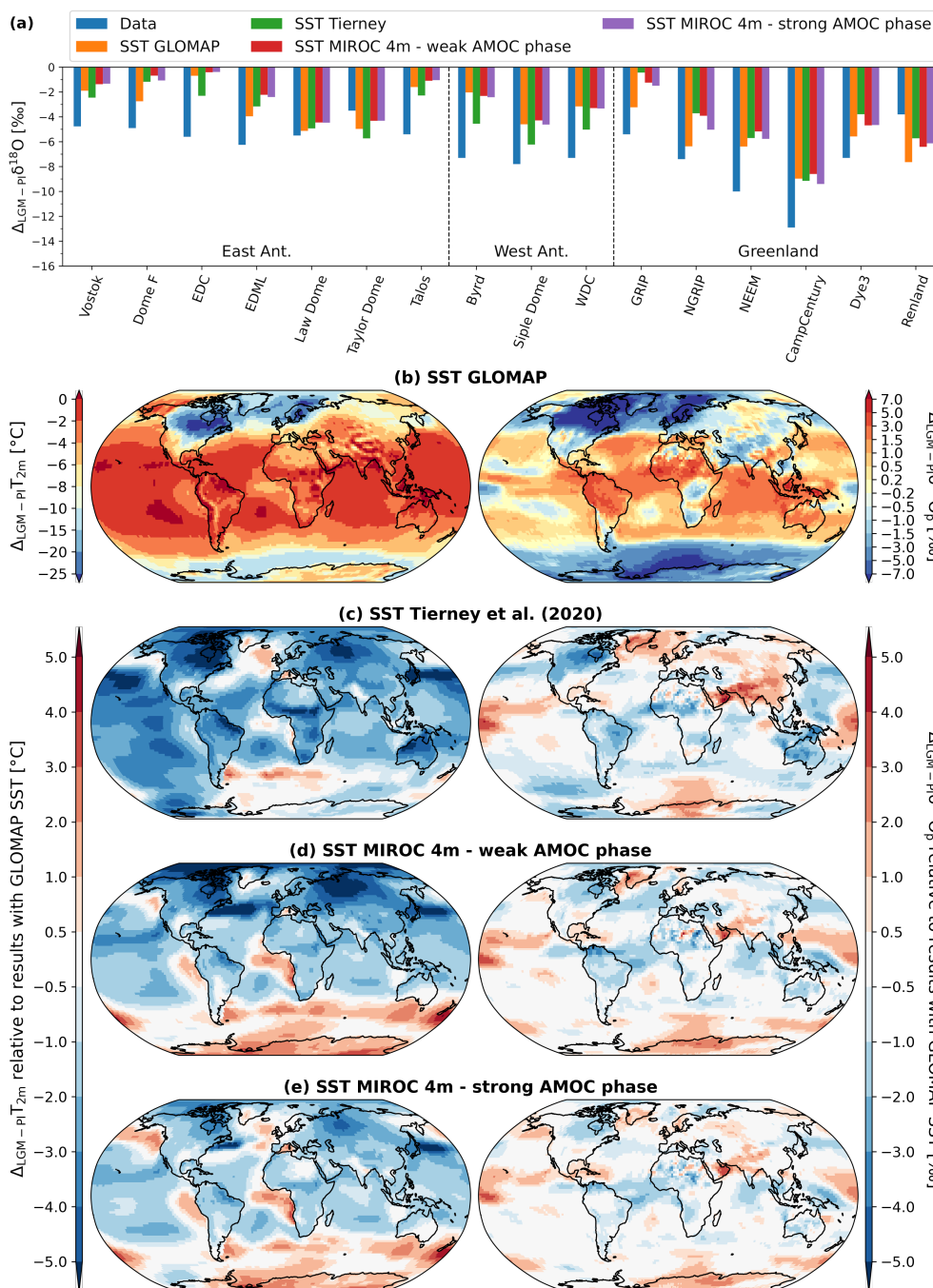


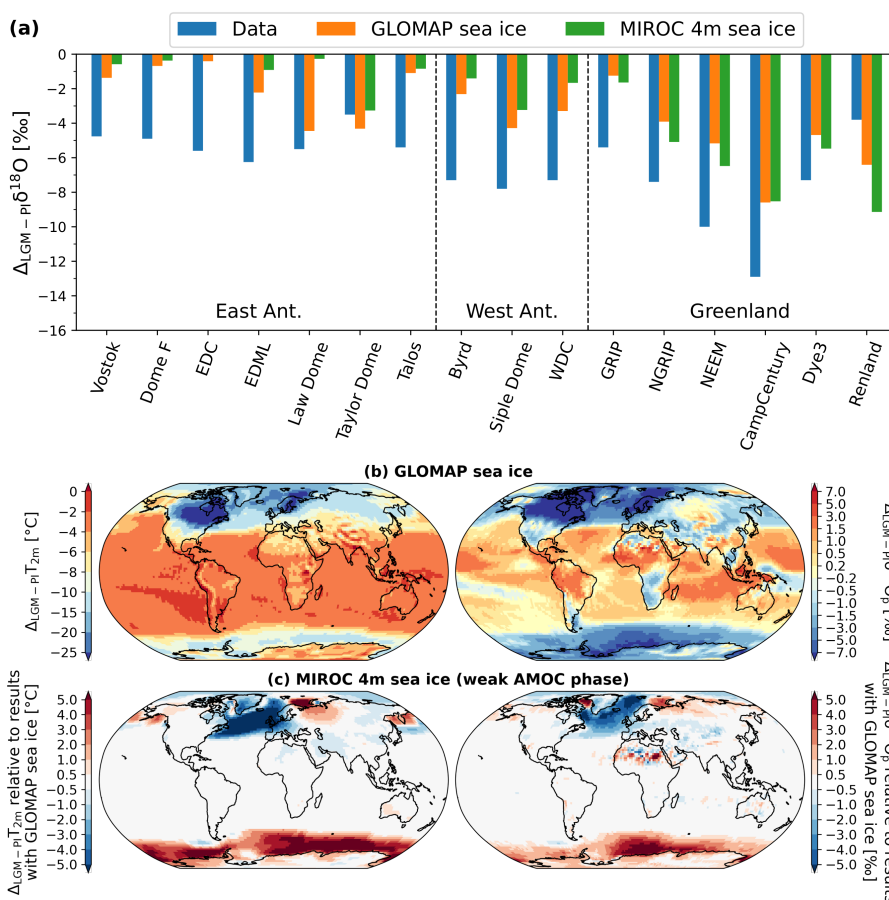
**Figure 5:** (a) Comparison of modeled anomalies in  $\delta^{18}\text{O}_{\text{sn}}$  between LGM and PI with  $\delta^{18}\text{O}$  anomalies measured in polar ice cores (blue bars). All modeled results are from simulations with the same sea ice boundary conditions from GLOMAP but with different SST forcings: GLOMAP (orange), Tierney et al. (2020) (green), MIROC 4m with weak LGM AMOC phase (red) and MIROC 4m with strong LGM AMOC phase (purple). (b) Modeled  $T_{2m}$  and  $\delta^{18}\text{O}_p$  changes between LGM and PI using GLOMAP SST (left and right maps, respectively). Maps in plots (c) to (e) show the impacts on  $T_{2m}$  and  $\delta^{18}\text{O}_p$  anomalies using the other SST boundary conditions. The values are expressed relative to the modeled results from (b).

300



### 3.3 Impacts of sea ice changes boundary conditions on the $\Delta_{\text{LGM-PI}}\delta^{18}\text{O}$ model-data agreement at polar ice core stations

To analyze the effects of sea ice boundary conditions on the modeled  $\delta^{18}\text{O}$  changes in polar regions between LGM and PI, we compare the results from the simulations using the same SST (here from the MIROC 4m simulation with the weak AMOC phase) but different sea ice area fraction fields: GLOMAP and MIROC 4m (i.e., LGM\_miroc4m\_sst\_glomap\_sic and LGM\_miroc4m\_sst\_and\_sic simulations, respectively). For all Antarctic ice core stations, a stronger depletion in  $\delta^{18}\text{O}_{\text{sn}}$  between LGM and PI is simulated with GLOMAP sea ice distribution (orange bars in Figure 6a). Except for Taylor Dome, a better agreement with isotopic observations is then found. The LGM sea ice from GLOMAP in the Southern Ocean is more extensive than the one from MIROC 4m (Figure 2). It has a huge impact on modeled  $T_{2\text{m}}$  anomalies over the Southern Ocean (between 2 and 10°C), and the simulated cooling is higher by 1 to 4°C in Western Antarctica and in coastal regions of the continent (left map of Figure 6c). As a consequence, higher LGM-PI anomalies in  $\delta^{18}\text{O}$  of precipitation and of snow are simulated: more than 5 ‰ over the Southern Ocean and around 1-2 ‰ on the continent, especially in the western part (right map of Figure 6c). The situation is opposite to that of the Arctic Ocean and Greenland with the sea ice from MIROC 4m (weak AMOC phase) being more extensive than the one from GLOMAP (Figure 2). Cooling is stronger by 5 to 10°C in the Arctic Ocean and from 0.5 to 5 °C in Greenland (left map of Figure 6c) when ECHAM6-wiso is forced by MIROC 4m sea ice boundary conditions, giving higher  $\delta^{18}\text{O}_p$  anomalies of up to 2 ‰ (right map of Figure 6c). The cooling is slightly lower near the Greenland coast because the LGM-PI sea ice change is more important in GLOMAP compared to MIROC 4m. This is due to the lower sea ice area fraction in grid cells near coastal areas in MIROC 4m (95-98% against 100% in GLOMAP, see section 2.2.2). This lower sea ice change in MIROC 4m combined with the isotopic content of snow on sea ice taken into account for sublimation processes in sea ice covered regions leads to a reduction of the LGM-PI  $\delta^{18}\text{O}_p$  changes in Baffin Bay (right map of Figure 6c). This aspect is investigated in detail in section 4.2. Finally, if the less extensive sea ice distribution from MIROC 4m under a strong AMOC phase is used to force ECHAM6-wiso, modeled  $\delta^{18}\text{O}_{\text{sn}}$  changes at Greenland ice core locations become smaller than the ones with GLOMAP sea ice, weakening the model-data agreement for this region (Figure S5).



325

**Figure 6:** (a) Comparison of modeled anomalies in  $\delta^{18}\text{O}_{\text{sn}}$  between LGM and PI with  $\delta^{18}\text{O}$  anomalies measured in polar ice cores (blue bars). Modeled results are from the simulations using the SST changes of MIROC 4m with weak LGM AMOC but different sea ice boundary conditions (GLOMAP and MIROC 4m with weak LGM AMOC phase in orange and green, respectively). (b) Modeled  $T_{2\text{m}}$  and  $\delta^{18}\text{O}_{\text{p}}$  changes between LGM and PI using GLOMAP sea ice (left and right maps, respectively). Maps in (c) show the impacts on  $T_{2\text{m}}$  and  $\delta^{18}\text{O}_{\text{p}}$  anomalies using sea ice from MIROC 4m instead. Values are expressed relative to the modeled results from (b).

330

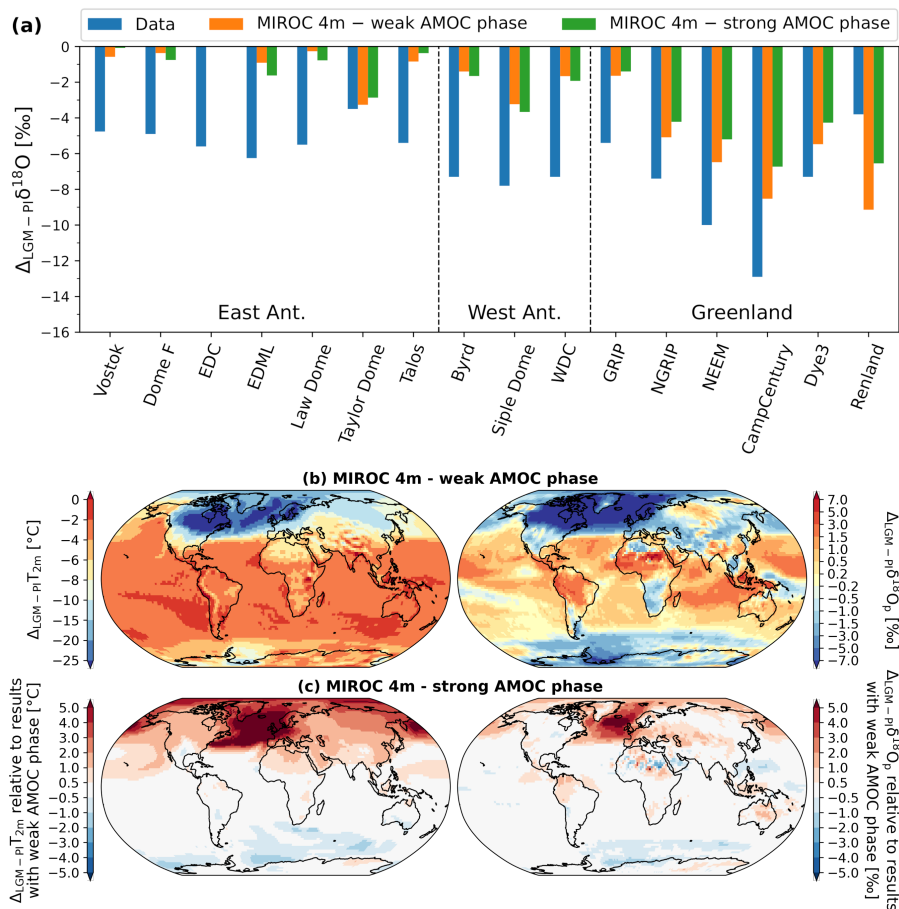
### 3.4 Impacts of LGM AMOC strength on the $\Delta_{\text{LGM-PI}}\delta^{18}\text{O}$ model-data agreement at polar ice core stations

Here, we investigate the impacts of AMOC strength on the modeled  $\Delta_{\text{LGM-PI}}\delta^{18}\text{O}$  in polar regions. For that, sea surface outputs (i.e., both SST and sea ice spatial distribution) from the MIROC 4m simulation with different LGM AMOC strengths are used as boundary conditions for ECHAM6-wiso. We focus first on the North Pole region because the AMOC strength mainly influences the climate of the Northern Hemisphere, as shown in SST and sea ice distributions used in this study (Figures 1 and 2). A weaker AMOC during LGM involves less heat transported in the north and thus lower LGM temperatures (i.e., larger cooling relative to PI), as shown in the left map of Figure 7c. A difference in  $T_{2\text{m}}$  of up to  $10^\circ\text{C}$  in the North Atlantic and Arctic Oceans is seen in the LGM\_miroc4m\_strong\_AMOC\_sst\_glomap\_sic and LGM\_miroc4m\_strong\_AMOC\_sst\_and\_sic simulations. Cooling in Greenland is reduced by 2-4  $^\circ\text{C}$  when the AMOC is increased. LGM to PI changes in  $\delta^{18}\text{O}$  in Greenland

340



is mainly controlled by this change in mean temperature with an increase in LGM  $\delta^{18}\text{O}_{\text{sn}}$  of between 1.2 and 2.5 ‰ at Greenland ice core stations for a stronger LGM AMOC (orange and green bar in Figure 7a). As ECHAM6-wiso generally underestimates the LGM-PI  $\delta^{18}\text{O}$  changes at the poles, a weaker AMOC generally improves the model-data agreement (blue and orange bars in Figure 7a). In the Southern Ocean and Antarctic regions, only small  $T_{2\text{m}}$  changes are simulated by ECHAM6-wiso due to a change in AMOC strength during LGM (left map of Figure 7c). As a consequence, modeled  $\Delta_{\text{LGM-PI}}\delta^{18}\text{O}_{\text{sn}}$  values are very similar between the 2 simulations (orange and green bars in Figure 7a). These small differences are due to the selection of the strong AMOC phase period in the middle of the peak in MIROC 4m simulation (see section 2.2.1). The impact of the period selection for the strong AMOC phase (e.g., the start or the end of the interstadial) on surface temperature and  $\delta^{18}\text{O}$  in Antarctica will be investigated more in detail in a future study. Finally, the changes of SST values alone due to AMOC strength variations change by only less than 1 ‰ of the modeled  $\Delta_{\text{LGM-PI}}\delta^{18}\text{O}_{\text{sn}}$  (red and purple bars in Figure 5a). This shows that the LGM to PI changes in sea ice distribution, related to the AMOC strength variations, have a large impact on modeled  $T_{2\text{m}}$  anomalies and consequently on the isotopic signals in the North Pole region.



355 **Figure 7:** (a) Comparison of modeled anomalies in  $\delta^{18}\text{O}_{\text{sn}}$  between LGM and PI with  $\delta^{18}\text{O}$  anomalies measured in polar ice cores (blue bars). Modeled results are from simulations using the sea surface boundary conditions from the MIROC 4m coupled





**simulations: LGM\_miroc4m\_sst\_and\_sic and LGM\_miroc4m\_strong\_AMOC\_sst\_and\_sic in orange and green, respectively. (b) Modeled  $T_{2m}$  and  $\delta^{18}O_p$  changes between LGM and PI using MIROC 4m (weak AMOC phase) sea surface boundary conditions (left and right maps, respectively). Maps in (c) show the impacts on  $T_{2m}$  and  $\delta^{18}O_p$  anomalies using sea surface boundary conditions from MIROC 4m at strong LGM AMOC phase. Values are expressed relative to the modeled results from (b).**

#### 360 4 Impacts of sea surface boundary conditions on $\delta^{18}O$ - $T_{2m}$ temporal slope for LGM-PI climate change

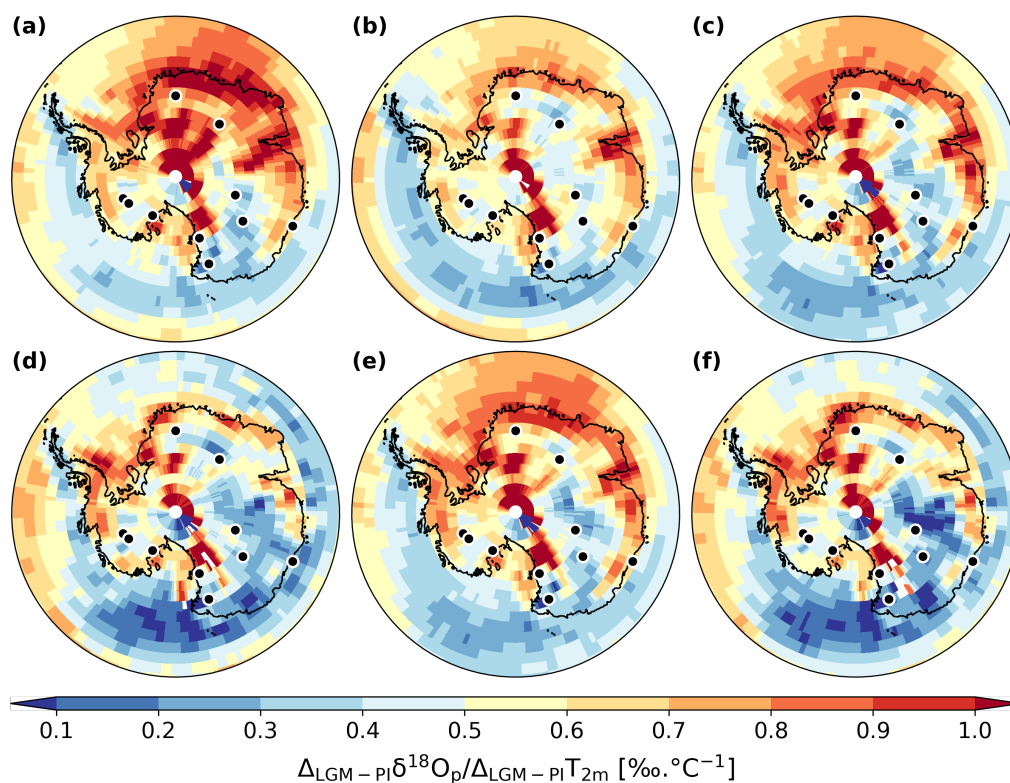
We have analyzed the effects of LGM to PI changes in SST and sea ice distribution on modeled  $\Delta_{LGM-PI}\delta^{18}O$  of precipitation and snow in the polar regions, as well as the impacts of the LGM AMOC strength. Next, we investigate the repercussions on modeled  $\delta^{18}O_p$ -  $T_{2m}$  temporal slopes. In other words, are  $T_{2m}$  and  $\delta^{18}O$  signals in the polar regions influenced in the same way by LGM to PI changes in SST and sea ice distribution? A correction for the prescribed glacial seawater change of 1 ‰ has  
365 been applied to LGM  $\delta^{18}O$  values before temporal slope calculation, according to equation 1 of Stenni et al. (2010).  $\delta^{18}O_p$  values in the polar regions might be biased by strong changes in the seasonality or intermittency of the precipitation rate (Sime et al., 2009; Kino et al., 2021). To take into account this effect, modeled  $T_{2m}$  values were weighted by the modeled monthly mean precipitation rates for the calculation of  $\delta^{18}O_p$ - $T_{2m}$  slopes (see Cauquoin et al., 2019b). As in Cauquoin et al. (2019b), the calculation of temporal slopes was restricted to grid cells where simulated temperatures are below +20°C for both PI and  
370 LGM. Moreover, we selected only the grid cells showing an absolute LGM-PI  $T_{2m}$  difference of at least of 0.5°C. As a comparative point, PI spatial  $\delta^{18}O_p$ - $T_{2m}$  slopes of 0.72 and 0.94 ‰ °C<sup>-1</sup> are modeled by ECHAM6-wiso in East and West Antarctic ice core stations, respectively (calculated by considering the 25 grid cells centered on each drill location, excluding the ocean grid points), consistent with the mean observed value of 0.8 ‰ °C<sup>-1</sup> (Masson-Delmotte et al., 2008) and previous modeling studies (Schmidt et al., 2007, Werner et al., 2018, Cauquoin et al., 2019b). For Greenland ice core stations, we find  
375 a modeled spatial slope of 0.71 ‰ °C<sup>-1</sup>, also in agreement with previous model results (Schmidt et al., 2007, Cauquoin et al., 2019b).

#### 4.1 Antarctica

The values of  $\delta^{18}O_p$ - $T_{2m}$  slope in East Antarctica are influenced in different ways by sea surface boundary conditions. LGM to PI changes in sea ice area fractions have a strong impact on the slopes in coastal regions, as shown by the comparison between  
380 the plots (c)-(d) and (e)-(f) of Figure 8. Law Dome ice core is representative of this impact, with a slope of 0.29 and 0.62 ‰ °C<sup>-1</sup> depending if MIROC 4m (LGM\_miroc4m\_sst\_and\_sic, Figure 8d) or GLOMAP (LGM\_miroc4m\_sst\_glomap\_sic, Figure 8c) sea ice is used, respectively. The change of sea ice forcing has only a small effect on the temporal slopes modeled by ECHAM6-wiso in the East Antarctic plateau. The most sensitive case is EDC where the temporal slope is increased from 0.19 to 0.3 ‰ °C<sup>-1</sup> when switching from MIROC 4m sea ice with a strong AMOC to the GLOMAP one (Figures 8f and 8e,  
385 respectively). On average, the modeled temporal  $\delta^{18}O_p$ - $T_{2m}$  slopes of East Antarctic ice core stations are increased by more than 25% when MIROC 4m sea ice (red and brown markers in Figure 10) is replaced by the GLOMAP one (green and purple markers in Figure 10) due mainly to the coastal stations (i.e., Law Dome, Taylor Dome, Talos Dome and, to a lesser extent,



EDML). The conclusions remain the same if instead of taking the averages of the slopes at ice cores stations, we use the average slope across the entire East Antarctic area (Figure S6). The SST forcings have various impacts on the temporal slopes simulated by ECHAM6-wiso. The SST forcing from Tierney et al. (2020) enhances the LGM cooling in the eastern part of the Southern Ocean area compared to other SST forcings (left map of Figure 5c). It influences both the LGM  $T_{2m}$  and  $\delta^{18}O_p$  in the same direction (i.e., toward lower values) but with different magnitudes at EDC, Vostok and Talos Dome. Temporal slopes at these stations are increased by 0.17, 0.11 and 0.08 ‰ °C<sup>-1</sup>, respectively, when ECHAM6-wiso is forced by SST from Tierney et al. (2020) instead of the one from GLOMAP. The higher cooling in the Atlantic sector of the Southern Ocean when ECHAM6-wiso is forced by GLOMAP SST (Figure 8a) makes the Antarctic temporal slope values higher between 0 and 90°E of longitude compared to the other simulations. It impacts especially the Dome Fuji and EDML ice core sites, where values of temporal  $\delta^{18}O_p$ - $T_{2m}$  slopes reach 0.8 and 0.67 ‰ °C<sup>-1</sup> (i.e., an increase of at least 60 and 34 %, respectively, compared to the other simulations). As a consequence, the modeled  $\delta^{18}O_p$ - $T_{2m}$  slopes in East Antarctic ice core stations are on average higher with GLOMAP SST forcing (blue marker in Figure 10). If all the East Antarctic area is considered, the forcing by the SST from GLOMAP increases the average  $\delta^{18}O_p$ - $T_{2m}$  slope by more than 20% compared to the other SST fields (Figure S6). Like in East Antarctica, a more extensive sea ice during LGM (i.e., GLOMAP) generally increases the modeled  $\delta^{18}O_p$ - $T_{2m}$  temporal slopes in West Antarctica. Except for the LGM simulation forced by Tierney et al. (2020) SST, the averages of temporal slopes for western Antarctic ice core stations are between 0.52 and 0.56 ‰ °C<sup>-1</sup> with GLOMAP sea ice, while they are between 0.45 and 0.52 ‰ °C<sup>-1</sup> if other sea ice forcings are used (Figure 10). This effect is larger in the Antarctic peninsula and on the coast of the Amundsen Sea (Figures 8 and 11), influencing the average slope values in the entire western part of the continent (Figure S6). The use of Tierney et al. (2020) SST instead of the GLOMAP one (Figures 8b and 8a, respectively) as forcing for ECHAM6-wiso makes the cooling in the extreme western part of the Southern Ocean and of the Antarctic continent higher by 1 to 4°C (left map of Figure 5c) but enhances the  $\delta^{18}O_p$  anomalies by only 3 ‰ at maximum (right map of Figure 5c). Therefore, the  $\delta^{18}O_p$ - $T_{2m}$  temporal slopes in Western Antarctica are on average decreased when ECHAM6-wiso is forced with SST from Tierney et al. (2020) instead of GLOMAP (orange and blue markers in Figures 10 and S6, summarized in Figure 11).



415 **Figure 8: Spatial distribution of  $\delta^{18}\text{O}_p$ - $T_{2m}$  temporal slope in Antarctica for LGM-PI changes according to our different ECHAM6-wiso simulations: (a) LGM\_GLOMAP, (b) LGM\_tierney2020, (c) LGM\_miroc4m\_sst\_glomap\_sic, (d) LGM\_miroc4m\_sst\_and\_sic, (e) LGM\_miroc4m\_strong\_AMOC\_sst\_glomap\_sic, and (f) LGM\_miroc4m\_strong\_AMOC\_sst\_and\_sic. The dots indicate the location of the ice core stations.**

## 4.2 Greenland

Using both SST and sea ice fields from GLOMAP as forcing for ECHAM6-wiso, we model higher  $\delta^{18}\text{O}_p$ - $T_{2m}$  temporal slope values at all Greenland ice core stations (Figure 9a) compared to all other simulations. This is generally true on the entire continent, too (blue marker in Figure S6). The average of the temporal slope values at ice core stations is  $0.62 \text{ } \text{‰} \text{ } ^\circ\text{C}^{-1}$  with GLOMAP sea surface boundary forcing (blue marker in Figure 10), and less than  $0.52 \text{ } \text{‰} \text{ } ^\circ\text{C}^{-1}$  in the other ECHAM6-wiso simulations. The influence of both SST and sea ice boundary fields explains this result.

The LGM-PI SST anomalies off the coast of Greenland are larger in GLOMAP compared to the other reconstructed and modeled SST fields (section 2.2.1), enhancing the cooling over North Atlantic Ocean (left maps of Figure 5) and so the LGM-PI anomalies in  $\delta^{18}\text{O}_p$  (maps on the right side of Figure 5). The water vapor from this region is transported further north over the Greenland Sea during summer when sea ice shrinks. In Greenland Sea, local SST change is small while  $\delta^{18}\text{O}_p$  anomalies are strong because of this water vapor transport. Then, the use of GLOMAP SST to force ECHAM6-wiso results in less cooling in the Greenland Sea area but stronger  $\delta^{18}\text{O}_p$  anomalies compared to ECHAM6-wiso simulations using other SST boundary



conditions (Figure 5). As a consequence, the modeled  $\delta^{18}\text{O}_p\text{-T}_{2m}$  temporal slopes are higher than  $1 \text{‰ } ^\circ\text{C}^{-1}$  over the Greenland  
430 Sea with GLOMAP SST (Figure 9a). The modeled slopes range only between 0.4 and  $0.8 \text{‰ } ^\circ\text{C}^{-1}$  in the other simulations  
(Figures 9b to 9f). This affects the temporal slope at the Renland coastal station, where a temporal slope of  $0.81 \text{‰ } ^\circ\text{C}^{-1}$  is  
simulated with GLOMAP SST, while this slope is below  $0.6 \text{‰ } ^\circ\text{C}^{-1}$  in other simulations. Moreover, the larger cooling off the  
coast of Greenland with GLOMAP SST influences the modeled  $\delta^{18}\text{O}_p\text{-T}_{2m}$  temporal slopes in inland Greenland ice core stations  
(Figure 9a) through changes in inland temperature (left maps of Figure 5) and also the inland transport of oceanic water vapor  
435 from the North Atlantic Ocean and the Baffin Bay.

The use of GLOMAP or MIROC 4m sea ice boundary as forcing for ECHAM6-wiso simulations lead to mixed results in terms  
of modeled  $\delta^{18}\text{O}_p\text{-T}_{2m}$  temporal slopes. The MIROC 4m sea ice in Greenland Sea shrinks less in summer compared to the one  
from GLOMAP (Figure 2). The effect on temperature is low but it enhances the LGM-PI anomalies in isotopic composition  
of precipitation over this area (Figure 6c), increasing the modeled  $\delta^{18}\text{O}_p\text{-T}_{2m}$  temporal slopes (Figures 9d and 9f). It has a slight  
440 effect on modeled temporal slopes ( $\sim 0.1 \text{‰ } ^\circ\text{C}^{-1}$ ) over the eastern coastal regions of Greenland, including the Renland station.  
In ECHAM6-wiso, the isotopic composition of sea ice surfaces also reflects the isotopic composition of snow deposited on  
this surface. Then the formation of new sea ice from PI to LGM acts as a positive feedback effect in the decrease of surrounding  
 $\delta^{18}\text{O}_p$ , leading to steeper modeled  $\delta^{18}\text{O}_p\text{-T}_{2m}$  temporal slopes (see text in Supplementary Material and Figure S7). Finally,  
ECHAM6-wiso forced with MIROC 4m sea ice, whose fractional areas are artificially lower (i.e., not 100% sea ice covered)  
445 in coastal grid cells, simulates lower  $\delta^{18}\text{O}_p\text{-T}_{2m}$  temporal slope values over Baffin Bay (between  $0.3$  and  $0.6 \text{‰ } ^\circ\text{C}^{-1}$ , Figures  
9d and 9f) compared to when the model is forced with GLOMAP sea ice (between  $0.7$  and  $1 \text{‰ } ^\circ\text{C}^{-1}$ , Figures 9c and 9e). If the  
MIROC 4m sea ice is corrected by setting sea ice fraction as 100% as in GLOMAP (see text in Supplementary Material and  
Figure S8), we obtain temporal slope values similar to those in the simulations forced by GLOMAP sea ice (Figure S9). It also  
slightly increases the  $\delta^{18}\text{O}_p\text{-T}_{2m}$  temporal slopes of inland ice core stations like NGRIP ( $0.53$  and  $0.67 \text{‰ } ^\circ\text{C}^{-1}$  with original  
450 (Figure 9d) and modified MIROC 4m sea ice, respectively). This result shows that the presence or absence of sea ice very near  
the coast has a large influence on the modeled temporal slopes in some Greenland ice core stations (Figure 11).

The AMOC strength during LGM influences both the SST and the sea ice distribution in the Arctic region. While stronger  
LGM AMOC weakens the isotopic model-data agreement in Greenland because the predominantly less extensive sea ice  
reduces the modeled surface cooling (see section 3.4), it generally does not impact the temporal slopes modeled by ECHAM6-  
455 wiso (red and brown lines in Figure 10) over inner Greenland. The ice core station that is most sensitive to the change in LGM  
AMOC strength is Renland, where the modeled  $\delta^{18}\text{O}_p\text{-T}_{2m}$  temporal slope is decreased from  $0.60$  to  $0.55 \text{‰ } ^\circ\text{C}^{-1}$  (Figures 9d  
and 9f).

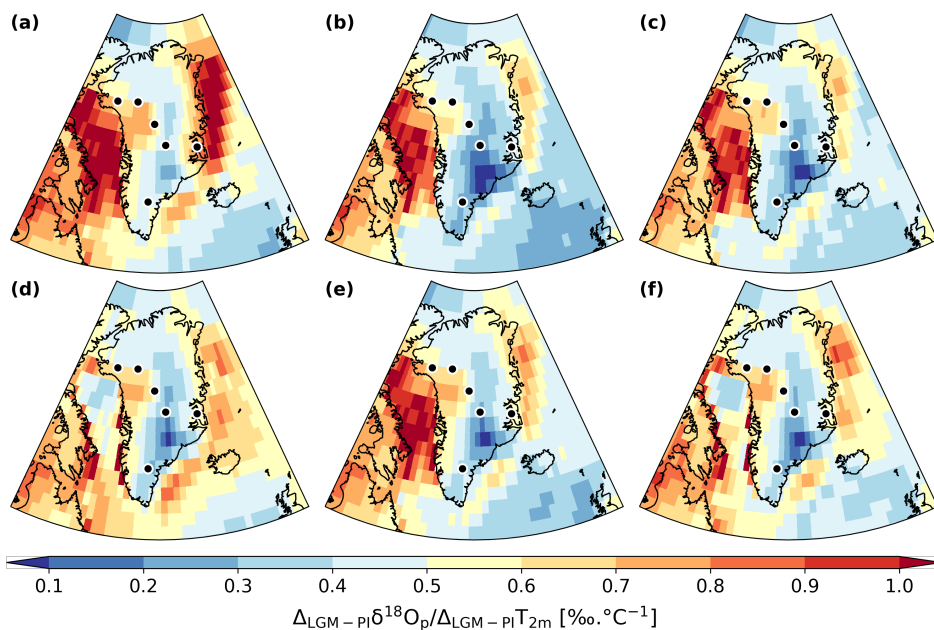


Figure 9: Same as Figure 8 but for the Greenland region.

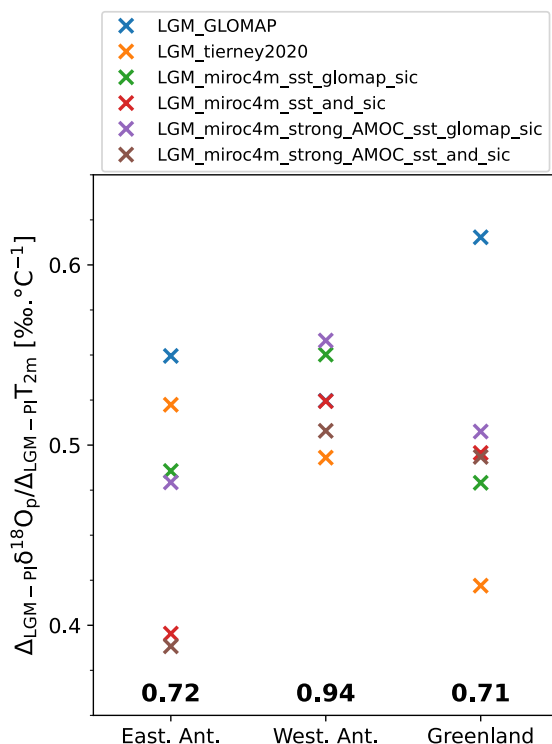


Figure 10: Average modeled values of  $\delta^{18}\text{O}_p\text{-}T_{2m}$  temporal slope for East Antarctic, West Antarctic and Greenland ice core stations according to our different simulations. Numbers in bold are the values of the corresponding modeled mean PI spatial slopes.

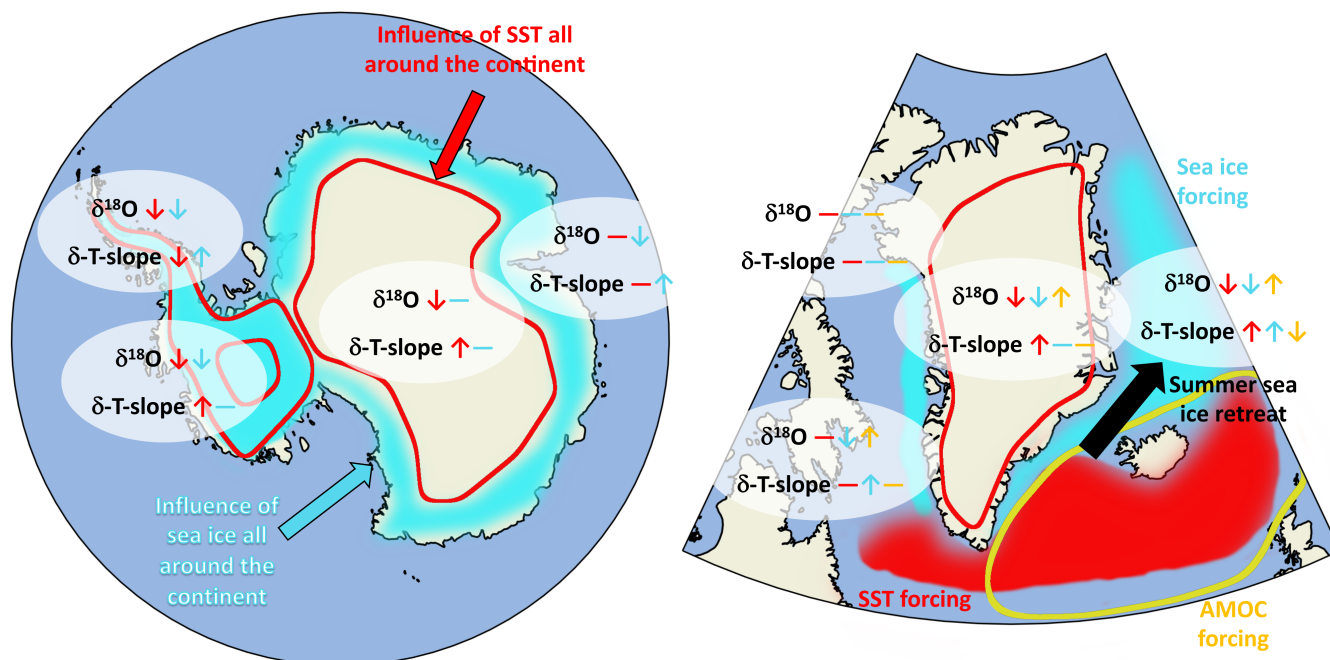


## 5 Conclusions and Perspectives

In this study, we raised the importance of sea surface boundary conditions on the relationship between near surface air  
465 temperature and  $\delta^{18}\text{O}_p$  for LGM to PI climate change. Figure 11 illustrates the main findings of our study. In East Antarctica,  
we noted the contrast between coastal regions and inland area in terms of control on the  $\delta^{18}\text{O}_p$ - $T_{2m}$  temporal slopes (left map  
of Figure 11). The coastal site Law Dome is greatly affected by the LGM sea ice extent, with more than double the value of  
the temporal slope and a better isotopic model-data agreement if GLOMAP sea ice is used instead of the MIROC 4m one  
(Figures 8c and 8d, respectively). On the other hand, no noteworthy change in the  $\delta^{18}\text{O}_p$ - $T_{2m}$  temporal slope is simulated  
470 regardless of the SST boundary conditions. A cooling larger by 1-2 °C in the Southern Ocean near Law Dome (Figure 5c)  
changes the temporal slope value at this station only by a small amount (less than  $0.05 \text{ } \text{‰} \cdot \text{°C}^{-1}$ ). The values of  $\delta^{18}\text{O}_p$ - $T_{2m}$   
temporal slopes in inland ice core stations like Dome F, EDML, EDC, Vostok and Talos are mainly controlled by the change  
of SST in our ECHAM6-wiso simulations. Stronger cooling in Atlantic sector of the Southern Ocean (GLOMAP) leads to  
steeper temporal slopes in Dome F and EDML (between 0 and 40° E). Similarly, stronger cooling in the eastern part of the  
475 Southern Ocean (Tierney et al., 2020) increases significantly the  $\delta^{18}\text{O}_p$ - $T_{2m}$  temporal slopes at EDC, Vostok and Talos. The  
steeper  $\delta^{18}\text{O}_p$ - $T_{2m}$  temporal slopes are accompanied by better isotopic model-data agreement at these ice core stations (Figure  
5a). The sea ice distribution can impact the  $\delta^{18}\text{O}_p$ - $T_{2m}$  temporal slopes at some inland stations, like EDML, but to a lesser  
extent compared to coastal regions. In West Antarctica, we showed that sea surface boundary conditions have a mixed effect  
on the  $\delta^{18}\text{O}_p$ - $T_{2m}$  temporal slopes (left map of Figure 11). For example, a steeper slope at WDC is simulated for more extensive  
480 sea ice in the western part of the Southern Ocean, while no significant effect on the  $\delta^{18}\text{O}_p$ - $T_{2m}$  temporal slope at Byrd, located  
very near WDC station, is seen. We note that a larger change in sea ice extent increases the mean  $\delta^{18}\text{O}_p$ - $T_{2m}$  temporal slope  
across the entire West Antarctic region (Figure S6). Larger sea surface cooling in the western part of the Southern Ocean  
slightly increases the  $\delta^{18}\text{O}_p$ - $T_{2m}$  temporal slopes at Byrd and WDC stations, and reduces it at Siple Dome. The lower change  
in  $\delta^{18}\text{O}_p$  compared to temperature could be explained by the influence of water vapor transport in this region. In Greenland,  
485 our modeled results demonstrate clearly that the  $\delta^{18}\text{O}_p$ - $T_{2m}$  temporal slopes in Greenland are influenced by the sea surface  
temperatures very near the coasts. The greater the LGM cooling off the coast of southeast Greenland, the larger the  $\delta^{18}\text{O}_p$ - $T_{2m}$   
temporal slopes (right map of Figure 11). The cooling in this region of the North Atlantic in the GLOMAP reconstruction is  
larger than in the Tierney et al. reconstruction or MIROC 4m model results, giving steeper modeled temporal slopes ( $0.62$  and  
 $0.42 \text{ } \text{‰} \cdot \text{°C}^{-1}$ , respectively, on average on all Greenland stations) and generally a better agreement with isotopic data (Figure  
490 5a). Similarly, the presence or absence of sea ice very near the coast can impact the modeled temporal slopes in some Greenland  
ice core stations, and has a large influence in Baffin Bay and the Greenland Sea. The large southern extent of the sea ice is not  
so important, as shown by the similar modeled temporal slope values using GLOMAP or MIROC 4m sea ice (weak AMOC  
phase). On the other hand, the seasonal variation of the sea ice distribution, especially its retreat in summer, influences the  
water vapor transport in this region and the modeled  $\delta^{18}\text{O}_p$ - $T_{2m}$  temporal slopes in the eastern part of the inner Greenland (right



495 map of Figure 11). Finally, while stronger LGM AMOC reduces the isotopic model-data agreement, it generally does not  
impact the temporal slopes modeled by ECHAM6-wiso over Greenland. Variations in the temporal slope values are located in  
the Greenland Sea, where the changes in surface temperature and sea ice distribution due to the AMOC strength mainly occur.  
For Antarctica, only small changes in surface temperature and  $\delta^{18}\text{O}$  are modeled by ECHAM6-wiso because the strong phase  
period was selected in the middle of the AMOC peak. The impact of the period selection for the strong AMOC phase, like the  
500 start or the end of the interstadial, will be investigated more in detail in a future study.



505 **Figure 11: Summary figure illustrating the influence of higher sea surface cooling, larger sea ice extent and stronger LGM AMOC (in red, cyan and yellow, respectively) on the modeled LGM  $\delta^{18}\text{O}$  and temporal  $\delta^{18}\text{O}_p\text{-T}_{2m}$  slopes in the Antarctic and Greenland regions (left and right, respectively). The up and down arrows indicate higher and lower values, respectively. The horizontal lines indicate no significant change.**

In Greenland, ECHAM6-wiso simulates on average  $\delta^{18}\text{O}_p\text{-T}_{2m}$  temporal slopes lower than the spatial one ( $0.71 \text{‰ } ^\circ\text{C}^{-1}$ , Figure 10), as already reported in previous studies (Buizert et al., 2014; Cauquoin et al., 2019b; Jouzel et al., 1999; Werner et al., 2000). In Antarctica, the ECHAM6-wiso modeled  $\delta^{18}\text{O}_p\text{-T}_{2m}$  temporal slopes for LGM-to-PI climate change are on average lower than the PI spatial slopes of the same model by at least 0.15 and  $0.38 \text{‰ } ^\circ\text{C}^{-1}$  for eastern and western ice core locations, respectively (Figure 10), regardless the simulation considered. By extension, we found much lower temporal slope values than the ones estimated by Buizert et al. (2021). We simulate a maximum temporal slope value of  $0.8 \text{‰ } ^\circ\text{C}^{-1}$  for Dome Fuji in the LGM\_GLOMAP simulation, while Buizert et al. (2021) found temporal slopes in Antarctic ice core stations ranging from 0.9 to  $1.4 \text{‰ } ^\circ\text{C}^{-1}$ , which are higher than the observed spatial  $\delta^{18}\text{O}_p\text{-T}_{2m}$  slope of  $0.8 \text{‰ } ^\circ\text{C}^{-1}$  (Masson-Delmotte et al., 2008). Compared to PMIP3 ice sheet reconstruction, the use of GLAC-1D to run LGM simulations reduces the isotopic model-data agreement for Antarctica (Figure S4). Also, the use of the old PMIP3 ice sheet reconstruction in ECHAM6-wiso increases the  
515



resulting modeled  $\delta^{18}\text{O}_p\text{-T}_{2m}$  temporal slopes (Figure S10) with mean values for East and West Antarctic ice core stations equal to 0.68 and 0.92 ‰ °C<sup>-1</sup>, respectively, which are closer to the modeled mean PI spatial slopes (0.71 and 0.94 ‰ °C<sup>-1</sup>, respectively) but still lower than the Buizert et al. (2021) results. So, the variability in LGM ice sheet reconstructions affects our modeled  $\delta^{18}\text{O}_p\text{-T}_{2m}$  temporal slopes for LGM-to-PI climate change in Antarctica, as already shown by Werner et al. (2018).  
520 On the other hand, we insist that the purpose of our study was to investigate the relative effects of sea surface conditions and AMOC strength the links between  $\delta^{18}\text{O}_p$  and near surface air temperature, regardless the agreement or disagreement with other slope reconstructions.

In addition to orography effects, fractionation during the sublimation of surface ice is not taken into account in ECHAM6-wiso as in many isotope-enabled AGCMs. This process would lead to a further decrease in the  $\delta^{18}\text{O}$  of water vapor in the polar  
525 regions, contributing to steeper modeled  $\delta^{18}\text{O}_p\text{-T}_{2m}$  temporal slopes in regions with low temperature. The mismatch between our model slopes and the reconstructed ones from Buizert et al. (2021) could be related to the representation of the atmospheric boundary layer and the related inversion temperature (Krinner et al., 1997; Masson-Delmotte et al., 2006; Cauquoin et al., 2019a), too. Still, despite these biases that potentially affect our modeled  $\delta^{18}\text{O}_p\text{-T}_{2m}$  temporal slopes for LGM-to-PI climate change, our ensemble of simulations provides information on how sea surface conditions partially control the links between  
530  $\delta^{18}\text{O}_p$  and near surface air temperature in polar regions.

Because only ECHAM6-wiso is used in this study, we cannot exclude the model-dependency of our results. So, the use of isotope-enabled AGCMs other than ECHAM6-wiso would be beneficial to confirm or refute our findings. A set of SST reconstructions for the LGM, based on both model results and observations, are now available. We raise the importance of providing sea ice cover reconstruction for this period too. The sea ice cover simulated by coupled GCMs for the LGM period  
535 takes various forms. An alternative reconstruction to the GLOMAP one, also based on observations, would help to better assess the impact of sea ice cover on the  $\delta^{18}\text{O}_p\text{-T}_{2m}$  relationship for LGM to PI climate change. As a first step, the focus of this study was to identify and quantify the important factors influencing the isotope-temperature relationship in the polar areas for the LGM to PI climate change. Future studies will investigate the evolution of this relationship along the whole of the last deglaciation. For that, an ensemble of equilibrium isotopic simulations using the sea surface and ice sheet boundary conditions  
540 from MIROC 4m for different time periods between the LGM and PI will be performed.

*Code availability.* The ECHAM model code is available under a version of the MPI-M software license agreement (<https://www.mpimet.mpg.de/en/science/models/license/>). The code of the isotopic version ECHAM6-wiso is available upon request on the AWI's GitLab repository (<https://gitlab.awi.de/mwerner/mpi-esm-wiso>).  
545

*Author contributions.* AC designed the model experiments and performed the simulations using the MIROC 4m sea surface boundary conditions with the help of AAO, TO and WLC. AC performed the simulations using the GLOMAP or Tierney et





al. sea surface boundary conditions with the help of MW and AP. AC and all the co-authors analyzed the model outputs. AC wrote the manuscript with contributions from all co-authors.

550

*Competing interests.* One of the co-author (André Paul) is editor in Climate of the Past.

*Acknowledgements.* This research was supported by JSPS KAKENHI Grant (17H06323) and by the German Federal Ministry of Education and Research (BMBF) as Research for Sustainability initiative (FONA). The ECHAM6-wiso simulations were performed at the Alfred Wegener Institute (AWI) supercomputing center. The MIROC 4m simulation used in this study was performed on the Earth Simulator 3 at Japan Agency for Marine-Earth Science and Technology (JAMSTEC).

555

## References

- Abe-Ouchi, A., Saito, F., Kawamura, K., Raymo, M. E., Okuno, J., Takahashi, K., and Blatter, H.: Insolation-driven 100,000-year glacial cycles and hysteresis of ice-sheet volume, *Nature*, 500, 190–193, <https://doi.org/10.1038/nature12374>, 2013.
- Blunier, T. and Brook, E. J.: Timing of Millennial-Scale Climate Change in Antarctica and Greenland During the Last Glacial Period, *Science*, 291, 109–112, <https://doi.org/10.1126/science.291.5501.109>, 2001.
- Brady, E., Stevenson, S., Bailey, D., Liu, Z., Noone, D., Nusbaumer, J., Otto-Bliesner, B. L., Tabor, C., Tomas, R., Wong, T., Zhang, J., and Zhu, J.: The Connected Isotopic Water Cycle in the Community Earth System Model Version 1, *J. Adv. Model. Earth Syst.*, 11, 2547–2566, <https://doi.org/10.1029/2019MS001663>, 2019.
- Briggs, R. D., Pollard, D., and Tarasov, L.: A data-constrained large ensemble analysis of Antarctic evolution since the Eemian, *Quat. Sci. Rev.*, 103, 91–115, <https://doi.org/10.1016/j.quascirev.2014.09.003>, 2014.
- Buizert, C., Gkinis, V., Severinghaus, J. P., He, F., Lecavalier, B. S., Kindler, P., Leuenberger, M., Carlson, A. E., Vinther, B., Masson-Delmotte, V., White, J. W. C., Liu, Z., Otto-Bliesner, B., and Brook, E. J.: Greenland temperature response to climate forcing during the last deglaciation, *Science*, 345, 1177–1180, <https://doi.org/10.1126/science.1254961>, 2014.
- Buizert, C., Fudge, T. J., Roberts, W. H. G., Steig, E. J., Sherriff-Tadano, S., Ritz, C., Lefebvre, E., Edwards, J., Kawamura, K., Oyabu, I., Motoyama, H., Kahle, E. C., Jones, T. R., Abe-Ouchi, A., Obase, T., Martin, C., Corr, H., Severinghaus, J. P., Beaudette, R., Epifanio, J. A., Brook, E. J., Martin, K., Chappellaz, J., Aoki, S., Nakazawa, T., Sowers, T. A., Alley, R. B., Ahn, J., Sigl, M., Severi, M., Dunbar, N. W., Svensson, A., Fegyveresi, J. M., He, C., Liu, Z., Zhu, J., Otto-Bliesner, B. L., Lipenkov, V. Y., Kageyama, M., and Schwander, J.: Antarctic surface temperature and elevation during the Last Glacial Maximum, *Science*, 372, 1097–1101, <https://doi.org/10.1126/science.abd2897>, 2021.

575



- Casado, M., Landais, A., Picard, G., Münch, T., Laepple, T., Stenni, B., Dreossi, G., Ekaykin, A., Arnaud, L., Genthon, C., Touzeau, A., Masson-Delmotte, V., and Jouzel, J.: Archival processes of the water stable isotope signal in East Antarctic ice cores, *The Cryosphere*, 12, 1745–1766, <https://doi.org/10.5194/tc-12-1745-2018>, 2018.
- Cauquoin, A. and Werner, M.: High-Resolution Nudged Isotope Modeling With ECHAM6-Wiso: Impacts of Updated Model Physics and ERA5 Reanalysis Data, *J. Adv. Model. Earth Syst.*, 13, <https://doi.org/10.1029/2021MS002532>, 2021.
- Cauquoin, A., Landais, A., Raisbeck, G. M., Jouzel, J., Bazin, L., Kageyama, M., Peterschmitt, J.-Y., Werner, M., Bard, E., and ASTER Team: Comparing past accumulation rate reconstructions in East Antarctic ice cores using  $^{10}\text{Be}$ , water isotopes and CMIP5-PMIP3 models, *Clim. Past*, 11, 355–367, <https://doi.org/10.5194/cp-11-355-2015>, 2015.
- Cauquoin, A., Risi, C., and Vignon, É.: Importance of the advection scheme for the simulation of water isotopes over Antarctica by atmospheric general circulation models: A case study for present-day and Last Glacial Maximum with LMDZ-iso, *Earth and Planet. Sci. Lett.*, 524, 115–131, <https://doi.org/10.1016/j.epsl.2019.115731>, 2019a.
- Cauquoin, A., Werner, M., and Lohmann, G.: Water isotopes – climate relationships for the mid-Holocene and preindustrial period simulated with an isotope-enabled version of MPI-ESM, *Clim. Past*, 15, 1913–1937, <https://doi.org/10.5194/cp-15-1913-2019>, 2019b.
- Comas-Bru, L., Harrison, S. P., Werner, M., Rehfeld, K., Scroxton, N., Veiga-Pires, C., and SISAL working group members: Evaluating model outputs using integrated global speleothem records of climate change since the last glacial, *Clim. Past*, 15, 1557–1579, <https://doi.org/10.5194/cp-15-1557-2019>, 2019.
- Comas-Bru, L., Rehfeld, K., Roesch, C., Amirnezhad-Mozhdehi, S., Harrison, S. P., Atsawawaranunt, K., Ahmad, S. M., Brahim, Y. A., Baker, A., Bosomworth, M., Breitenbach, S. F. M., Burstyn, Y., Columbu, A., Deininger, M., Demény, A., Dixon, B., Fohlmeister, J., Hatvani, I. G., Hu, J., Kaushal, N., Kern, Z., Labuhn, I., Lechleitner, F. A., Lorrey, A., Martrat, B., Novello, V. F., Oster, J., Pérez-Mejías, C., Scholz, D., Scroxton, N., Sinha, N., Ward, B. M., Warken, S., and Zhang, H.: SISALv2: a comprehensive speleothem isotope database with multiple age–depth models, *Earth Syst. Sci. Data*, 12, 2579–2606, <https://doi.org/10.5194/essd-12-2579-2020>, 2020.
- Craig, H.: Isotopic Variations in Meteoric Waters, *Science*, 133, 1702–1703, <https://doi.org/10.1126/science.133.3465.1702>, 1961.
- Craig, H. and Gordon, L. I.: Deuterium and oxygen 18 variation in the ocean and marine atmosphere, in: *Stable Isotopes in Oceanographic Studies and Paleotemperatures*, edited by Tongiogi, E., pp. 9–130, Consiglio nazionale delle ricerche, Laboratorio de geologia nucleare, Spoleto, Italy, 1965.
- Dansgaard, W.: Stable isotopes in precipitation, *Tellus*, 16, 436–468, <https://doi.org/10.3402/tellusa.v16i4.8993>, 1964.
- Dreybrodt, W. and Scholz, D.: Climatic dependence of stable carbon and oxygen isotope signals recorded in speleothems: From soil water to speleothem calcite, *Geochim. Cosmochim. Ac.*, 75, 734–752, <https://doi.org/10.1016/j.gca.2010.11.002>, 2011.
- Giorgetta, M. A., Jungclaus, J., Reick, C. H., Legutke, S., Bader, J., Böttinger, M., Brovkin, V., Crueger, T., Esch, M., Fieg, K., Glushak, K., Gayler, V., Haak, H., Hollweg, H.-D., Ilyina, T., Kinne, S., Kornbluh, L., Matei, D., Mauritsen, T.,



- 615 Mikolajewicz, U., Mueller, W., Notz, D., Pithan, F., Raddatz, T., Rast, S., Redler, R., Roeckner, E., Schmidt, H.,  
Schnur, R., Segschneider, J., Six, K. D., Stockhause, M., Timmreck, C., Wegner, J., Widmann, H., Wieners, K.-H.,  
Claussen, M., Marotzke, J., and Stevens, B.: Climate and carbon cycle changes from 1850 to 2100 in MPI-ESM  
simulations for the Coupled Model Intercomparison Project phase 5, *J. Adv. Model. Earth Syst.*, 5, 572–597,  
<https://doi.org/10.1002/jame.20038>, 2013.
- Guillevic, M., Bazin, L., Landais, A., Kindler, P., Orsi, A., Masson-Delmotte, V., Blunier, T., Buchardt, S. L., Capron, E.,  
Leuenberger, M., Martinerie, P., Prié, F., and Vinther, B. M.: Spatial gradients of temperature, accumulation and  $\delta^{18}\text{O}$ -  
ice in Greenland over a series of Dansgaard–Oeschger events, *Clim. Past*, 9, 1029–1051, <https://doi.org/10.5194/cp-9-1029-2013>, 2013.
- 620 Jouzel, J.: Calibrating the Isotopic Paleothermometer, *Science*, 286, 910–911, <https://doi.org/10.1126/science.286.5441.910>,  
1999.
- Jouzel, J.: A brief history of ice core science over the last 50 yr, *Clim. Past*, 9, 2525–2547, <https://doi.org/10.5194/cp-9-2525-2013>, 2013.
- 625 Jouzel, J., Masson-Delmotte, V., Cattani, O., Dreyfus, G., Falourd, S., Hoffmann, G., Minster, B., Nouet, J., Barnola, J.-M.,  
Blunier, T., Chappellaz, J., Fischer, H., Gallet, J. C., Johnsen, S., Leuenberger, M., Loulergue, L., Luethi, D., Oerter,  
H., Parrenin, F., Raisbeck, G., Raynaud, D., Schilt, A., Schwander, J., Delmo, E., Souchez, R., Spahni, R., Stauffer, B.,  
Steffensen, J. P., Stenni, B., Stocker, T. F., Tison, J. L., Werner, M., and Wolff, E.: Orbital and Millennial Antarctic  
Climate Variability over the Past 800,000 Years, *Science*, 317, 793–796, <https://doi.org/10.1126/science.1141038>,  
630 2007.
- Kageyama, M., Braconnot, P., Harrison, S. P., Haywood, A. M., Jungclauss, J. H., Otto-Bliesner, B. L., Peterschmitt, J.-Y.,  
Abe-Ouchi, A., Albani, S., Bartlein, P. J., Brierley, C., Crucifix, M., Dolan, A., Fernandez-Donado, L., Fischer, H.,  
Hopcroft, P. O., Ivanovic, R. F., Lambert, F., Lunt, D. J., Mahowald, N. M., Peltier, W. R., Phipps, S. J., Roche, D. M.,  
Schmidt, G. A., Tarasov, L., Valdes, P. J., Zhang, Q., and Zhou, T.: The PMIP4 contribution to CMIP6 – Part 1:  
635 Overview and over-arching analysis plan, *Geosci. Model Dev.*, 11, 1033–1057, <https://doi.org/10.5194/gmd-11-1033-2018>, 2018.
- Kageyama, M., Harrison, S. P., Kapsch, M.-L., Lofverstrom, M., Lora, J. M., Mikolajewicz, U., Sherriff-Tadano, S., Vadsaria,  
T., Abe-Ouchi, A., Bouttes, N., Chandan, D., Gregoire, L. J., Ivanovic, R. F., Izumi, K., LeGrande, A. N., Lhardy, F.,  
Lohmann, G., Morozova, P. A., Ohgaito, R., Paul, A., Peltier, W. R., Poulsen, C. J., Quiquet, A., Roche, D. M., Shi,  
640 X., Tierney, J. E., Valdes, P. J., Volodin, E., and Zhu, J.: The PMIP4 Last Glacial Maximum experiments: preliminary  
results and comparison with the PMIP3 simulations, *Clim. Past*, 17, 1065–1089, <https://doi.org/10.5194/cp-17-1065-2021>, 2021.
- Kawamura, K., Parrenin, F., Lisiecki, L., Uemura, R., Vimeux, F., Severinghaus, J. P., Hutterli, M. A., Nakazawa, T., Aoki,  
S., Jouzel, J., Raymo, M. E., Matsumoto, K., Nakata, H., Motoyama, H., Fujita, S., Goto-Azuma, K., Fujii, Y., and



- 645 Watanabe, O.: Northern Hemisphere forcing of climatic cycles in Antarctica over the past 360,000 years, *Nature*, 448, 912–916, <https://doi.org/10.1038/nature06015>, 2007.
- Kino, K., Okazaki, A., Cauquoin, A., and Yoshimura, K.: Contribution of the Southern Annular Mode to Variations in Water Isotopes of Daily Precipitation at Dome Fuji, East Antarctica, *J. Geophys. Res. Atmos.*, 126, <https://doi.org/10.1029/2021JD035397>, 2021.
- 650 Krinner, G., Genthon, C., Li, Z.-X., and Le Van, P.: Studies of the Antarctic climate with a stretched-grid general circulation model, *J. Geophys. Res. Atmos.*, 102, 13 731–13 745, <https://doi.org/10.1029/96JD03356>, 1997.
- Landais, A., Masson-Delmotte, V., Stenni, B., Selmo, E., Roche, D. M., Jouzel, J., Lambert, F., Guillevic, M., Bazin, L., Arzel, O., Vinther, B., Gkinis, V., and Popp, T.: A review of the bipolar see-saw from synchronized and high resolution ice core water stable isotope records from Greenland and East Antarctica, *Quat. Sci. Rev.*, 114, 18–32, <https://doi.org/10.1016/j.quascirev.2015.01.031>, 2015.
- 655 Lee, J.-E., Fung, I., DePaolo, D. J., and Otto-Bliesner, B.: Water isotopes during the Last Glacial Maximum: New general circulation model calculations, *J. Geophys. Res.*, 113, D19 109, <https://doi.org/10.1029/2008JD009859>, 2008.
- LeGrande, A. N. and Schmidt, G. A.: Global gridded data set of the oxygen isotopic composition in seawater, *Geophys. Res. Lett.*, 33, <https://doi.org/10.1029/2006gl026011>, 2006.
- 660 Masson-Delmotte, V., Kageyama, M., Braconnot, P., Charbit, S., Krinner, G., Ritz, C., Guilyardi, E., Jouzel, J., Abe-Ouchi, A., Crucifix, M., Gladstone, R. M., Hewitt, C. D., Kitoh, A., LeGrande, A. N., Marti, O., Merkel, U., Motoi, T., Ohgaito, R., Otto-Bliesner, B., Peltier, W. R., Ross, I., Valdes, P. J., Vettoretti, G., Weber, S. L., Wolk, F., and Yu, Y.: Past and future polar amplification of climate change: climate model intercomparisons and ice-core constraints, *Clim. Dynam.*, 26, 513–529, <https://doi.org/10.1007/s00382-005-0081-9>, 2006.
- 665 Masson-Delmotte, V., Hou, S., Ekaykin, A., Jouzel, J., Aristarain, A., Bernardo, R. T., Bromwich, D., Cattani, O., Delmotte, M., Falourd, S., Frezzotti, M., Gallée, H., Genoni, L., Isaksson, E., Landais, A., Helsen, M., Hoffmann, G., Lopez, J., Morgan, V., Motoyama, H., Noone, D., Oerter, H., Petit, J. R., Royer, A., Uemura, R., Schmidt, G. A., Schlosser, E., Simões, J. C., Steig, E., Stenni, B., Stievenard, M., van den Broeke, M., van de Wal, R., van de Berg, W.-J., Vimeux, F., and White, J. W. C.: A review of Antarctic surface snow isotopic composition: observations, atmospheric circulation and isotopic modelling, *J. Climate*, 21, 3359–3387, <https://doi.org/10.1175/2007JCLI2139.1>, 2008.
- 670 Mauritsen, T., Bader, J., Becker, T., Behrens, J., Bittner, M., Brokopf, R., Brovkin, V., Claussen, M., Crueger, T., Esch, M., Fast, I., Fiedler, S., Fläschner, D., Gayler, V., Giorgetta, M., Goll, D. S., Haak, H., Hagemann, S., Hedemann, C., Hohenegger, C., Ilyina, T., Jahns, T., la Cuesta, D. J.-d., Jungclaus, J., Kleinen, T., Kloster, S., Kracher, D., Kinne, S., Kleberg, D., Lasslop, G., Kornbluh, L., Marotzke, J., Matei, D., Meraner, K., Mikolajewicz, U., Modali, K., Möbis, B., Müller, W. A., Nabel, J. E. M. S., Nam, C. C. W., Notz, D., Nyawira, S.-S., Paulsen, H., Peters, K., Pincus, R., Pohlmann, H., Pongratz, J., Popp, M., Raddatz, T. J., Rast, S., Redler, R., Reick, C. H., Rohrschneider, T., Schemann, V., Schmidt, H., Schnur, R., Schulzweida, U., Six, K. D., Stein, L., Stemmler, I., Stevens, B., Storch, J.-S., Tian, F., Voigt, A., Vrese, P., Wieners, K.-H., Wilkenskjaeld, S., Winkler, A., and Roeckner, E.: Developments in the MPI- M



- 680 Earth System Model version 1.2 (MPI-ESM1.2) and Its Response to Increasing CO<sub>2</sub>, *J. Adv. Model. Earth Syst.*, 11, 998–1038, <https://doi.org/10.1029/2018ms001400>, 2019.
- NEEM Community Members: Eemian interglacial reconstructed from a Greenland folded ice core, *Nature*, 493, 489–494, <https://doi.org/10.1038/nature11789>, 2013.
- Noone, D. and Simmonds, I.: Sea ice control of water isotope transport to Antarctica and implications for ice core interpretation, *J. Geophys. Res. Atmos.*, 109, D07 105, <https://doi.org/10.1029/2003jd004228>, 2004.
- 685 North Greenland Ice Core Project members: High-resolution record of Northern Hemisphere climate extending into the last interglacial period, *Nature*, 431, 147–151, <https://doi.org/10.1038/nature02805>, 2004.
- Obase, T. and Abe-Ouchi, A.: Abrupt Bølling-Allerød Warming Simulated under Gradual Forcing of the Last Deglaciation, *Geophys. Res. Lett.*, 46, 11 397–11 405, <https://doi.org/10.1029/2019GL084675>, 2019.
- Paul, A., Mulitza, S., Stein, R., and Werner, M.: A global climatology of the ocean surface during the Last Glacial Maximum mapped on a regular grid (GLOMAP), *Clim. Past*, 17, 805–824, <https://doi.org/10.5194/cp-17-805-2021>, 2021.
- 690 Schmidt, G. A., LeGrande, A. N., and Hoffmann, G.: Water isotope expressions of intrinsic and forced variability in a coupled ocean- atmosphere model, *J. Geophys. Res.*, 112, D10103, <https://doi.org/10.1029/2006JD007781>, 2007.
- Schüpbach, S., Fischer, H., Bigler, M., Erhardt, T., Gfeller, G., Leuenberger, D., Mini, O., Mulvaney, R., Abram, N. J., Fleet, L., Frey, M. M., Thomas, E., Svensson, A., Dahl-Jensen, D., Kettner, E., Kjaer, H., Seierstad, I., Steffensen, J. P., Rasmussen, S. O., Vallelonga, P., Winstrup, M., Wegner, A., Twarloh, B., Wolff, K., Schmidt, K., Goto-Azuma, K., Kuramoto, T., Hirabayashi, M., Uetake, J., Zheng, J., Bourgeois, J., Fisher, D., Zhiheng, D., Xiao, C., Legrand, M., Spolaor, A., Gabrieli, J., Barbante, C., Kang, J.-H., Hur, S. D., Hong, S. B., Hwang, H. J., Hong, S., Hansson, M., Iizuka, Y., Oyabu, I., Muscheler, R., Adolphi, F., Maselli, O., McConnell, J., and Wolff, E. W.: Greenland records of aerosol source and atmospheric lifetime changes from the Eemian to the Holocene, *Nat. Commun.*, 9, 1476, <https://doi.org/10.1038/s41467-018-03924-3>, 2018.
- 695 700 Sime, L. C., Wolff, E. W., Oliver, K. I. C., and Tindall, J. C.: Evidence for warmer interglacials in East Antarctic ice cores, *Nature*, 462, 342–345, <https://doi.org/10.1038/nature08564>, 2009.
- Steig, E. J., Morse, D. L., Waddington, E. D., Stuiver, M., Grootes, P. M., Mayewski, P. A., Twickler, M. S., and Whitlow, S. I.: Wisconsinan and Holocene climate history from an ice core at Taylor Dome, western Ross embayment, Antarctica, *Geografiska Annaler*, 82A, 213–235, <https://doi.org/10.1111/j.0435-3676.2000.00122.x>, 2000.
- 705 Stenni, B., Masson-Delmotte, V., Selmo, E., Oerter, H., Meyer, H., Röthlisberger, R., Jouzel, J., Cattani, O., Falourd, S., Fischer, H., Hoffmann, G., Iacumin, P., Johnsen, S. J., Minster, B., and Udisti, R.: The deuterium excess records of EPICA Dome C and Dronning Maud Land ice cores (East Antarctica), *Quat. Sci. Rev.*, 29, 146–159, <https://doi.org/10.1016/j.quascirev.2009.10.009>, 2010.
- 710 Stenni, B., Buiron, D., Frezzotti, M., Albani, S., Barbante, C., Bard, E., Barnola, J. M., Baroni, M., Baumgartner, M., Bonazza, M., Capron, E., Castellano, E., Chappellaz, J., Delmonte, B., Falourd, S., Genoni, L., Iacumin, P., Jouzel, J., Kipfstuhl, S., Landais, A., Lemieux-Dudon, B., Maggi, V., Masson-Delmotte, V., Mazzola, C., Minster, B., Montagnat, M.,



- 715 Mulvaney, R., Narcisi, B., Oerter, H., Parrenin, F., Petit, J. R., Ritz, C., Scarchilli, C., Schilt, A., Schüpbach, S., Schwander, J., Selmo, E., Severi, M., Stocker, T. F., and Udisti, R.: Expression of the bipolar see-saw in Antarctic climate records during the last deglaciation, *Nat. Geosci.*, 4, 46–49, <https://doi.org/10.1038/ngeo1026>, 2011.
- Stevens, B., Giorgetta, M., Esch, M., Mauritsen, T., Crueger, T., Rast, S., Salzmann, M., Schmidt, H., Bader, J., Block, K., Brokopf, R., Fast, I., Kinne, S., Kornbluh, L., Lohmann, U., Pincus, R., Reichler, T., and Roeckner, E.: Atmospheric component of the MPI-M Earth System Model: ECHAM6, *J. Adv. Model. Earth Syst.*, 5, 146–172, <https://doi.org/10.1002/jame.20015>, 2013.
- 720 Tarasov, L. and Peltier, W. R.: Greenland glacial history and local geodynamic consequences, *Geophysical Journal International*, 150, 198–229, <https://doi.org/10.1046/j.1365-246X.2002.01702.x>, 2002.
- Tarasov, L., Dyke, A. S., Neal, R. M., and Peltier, W. R.: A data-calibrated distribution of deglacial chronologies for the North American ice complex from glaciological modeling, *Earth and Planet. Sci. Lett.*, 315–316, 30–40, <https://doi.org/10.1016/j.epsl.2011.09.010>, 2012.
- 725 Tarasov, L., Hughes, A., Gyllencreutz, R., Lohne, O. S., Mangerud, J., and Svendsen, J.-I.: The global GLAC-1c deglaciation chronology, meltwater pulse 1-a, and a question of missing ice, in: *IGS Symposium on Contribution of Glaciers and Ice Sheets to Sea-Level Change*, 2014.
- Tierney, J. E., Zhu, J., King, J., Malevich, S. B., Hakim, G. J., and Poulsen, C. J.: Glacial cooling and climate sensitivity revisited, *Nature*, 584, 569–573, <https://doi.org/10.1038/s41586-020-2617-x>, 2020.
- 730 Vinther, B. M., Andersen, K. K., Jones, P. D., Briffa, K. R., and Cappelen, J.: Extending Greenland temperature records into the late eighteenth century, *J. Geophys. Res.*, 111, D11 105, <https://doi.org/10.1029/2005jd006810>, 2006.
- Vinther, B. M., Buchardt, S. L., Clausen, H. B., Dahl-Jensen, D., Johnsen, S. J., Fisher, D. A., Koerner, R. M., Raynaud, D., Lipenkov, V., Andersen, K. K., Blunier, T., Rasmussen, S. O., Steffensen, J. P., and Svensson, A. M.: Holocene thinning of the Greenland ice sheet, *Nature*, 461, 385–388, <https://doi.org/10.1038/nature08355>, 2009.
- 735 Wackerbarth, A., Scholz, D., Fohlmeister, J., and Mangini, A.: Modelling the  $\delta^{18}\text{O}$  value of cave drip water and speleothem calcite, *Earth and Planet. Sci. Lett.*, 299, 387–397, <https://doi.org/10.1016/j.epsl.2010.09.019>, 2010.
- WAIS Divide Project Members: Onset of deglacial warming in West Antarctica driven by local orbital forcing, *Nature*, 500, 440–444, <https://doi.org/10.1038/nature12376>, 2013.
- Werner, M., Mikolajewicz, U., Heimann, M., and Hoffmann, G.: Borehole versus isotope temperatures on Greenland: Seasonality does matter, *Geophys. Res. Lett.*, 27, 723–726, <https://doi.org/10.1029/1999gl006075>, 2000.
- 740 Werner, M., Jouzel, J., Masson-Delmotte, V., and Lohmann, G.: Reconciling glacial Antarctic water stable isotopes with ice sheet topography and the isotopic paleothermometer, *Nat. Commun.*, 9, <https://doi.org/10.1038/s41467-018-05430-y>, 2018.